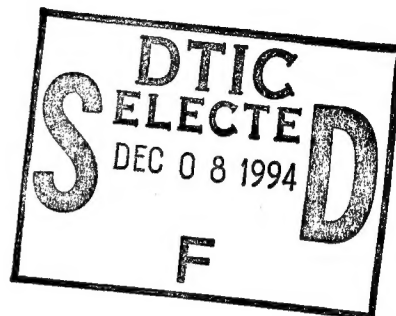


# NAVAL POSTGRADUATE SCHOOL

## Monterey, California



\*Original contains color  
plates: All DTIC reproductions  
will be in black and  
white\*

## THESIS

### DEEP CONVECTION IN THE MEDITERRANEAN SEA

by

Bernard Arata

September 1994

Thesis Advisor:

Roland W. Garwood, Jr.

Approved for public release; distribution is unlimited.

DTIC QUALITY INSPECTED 5

19941201 042

**REPORT DOCUMENTATION PAGE**Form Approved OMB  
No. 0704-0188

Public reporting burden for this collection of information is estimated to average 1 hour per response, including the time for reviewing instruction, searching existing data sources, gathering and maintaining the data needed, and completing and reviewing the collection of information. Send comments regarding this burden estimate or any other aspect of this collection of information, including suggestions for reducing this burden, to Washington headquarters Services, Directorate for Information Operations and Reports, 1215 Jefferson Davis Highway, Suite 1204, Arlington, VA 22202-4302, and to the Office of Management and Budget, Paperwork Reduction Project (0704-0188) Washington DC 20503.

1. AGENCY USE ONLY (Leave blank)	2. REPORT DATE September, 1994	3. REPORT TYPE AND DATES COVERED Master's Thesis	
4. TITLE AND SUBTITLE DEEP CONVECTION IN THE MEDITERRANEAN SEA		5. FUNDING NUMBERS	
6. AUTHOR(S) Arata, Bernard, H.			
7. PERFORMING ORGANIZATION NAME(S) AND ADDRESS(ES) Naval Postgraduate School Monterey CA 93943-5000		8. PERFORMING ORGANIZATION	
9. SPONSORING/MONITORING AGENCY NAME(S) AND ADDRESS(ES)		10. SPONSORING/MONITORING AGENCY REPORT NUMBER	
11. SUPPLEMENTARY NOTES The views expressed in this thesis are those of the author and do not reflect the official policy or position of the Department of Defense or the U.S. Government.			
12a. DISTRIBUTION/AVAILABILITY STATEMENT Approved for public release; distribution is unlimited.		12b. DISTRIBUTION CODE A	
13. ABSTRACT (maximum 200 words)  It is now understood that deep convection in the ocean plays a dominant role in determining the climate of the world's oceans. Recent theoretical advances in explaining oceanic convection need to be tested by real observations. Satellite observations of deep convection regions may be a promising new tool in studying this phenomenon. This thesis examines deep convection events in two ways: <ul style="list-style-type: none"><li>• To assess the characteristic elements of a deep convection event using two different prediction models based upon the turbulent kinetic energy budget.</li><li>• To attempt to observe deep convection phenomena signals in altimeter data.</li></ul> In 1987, a deep convection event was observed in the northwestern Mediterranean sea (Schott and Leaman 1991). These data, combined with GEOSAT altimeter data, were used to verify the Kraus and Turner and the Naval Postgraduate School mixed layer model predictions of the time evolution of temperature, salinity and mixed layer depth. Both models predicted final values similar to the observations, but model tuning was required to reproduce the observed rapid mixed-layer deepening. The interpolated altimeter field does not allow identification with confidence of the Mediterranean convection area. However, a locally persistent feature and the mean winter sea surface topography field agree with in-situ observations and do provide some indication about where and when the convection process occurs.			
14. SUBJECT TERMS Deep Convection in the Ocean, Hydrographic Data, Kraus and Turner Model, Naval Postgraduate School Model, Satellite Data, Correction of Satellite Data, Multiquadric Interpolation, Satellite Data Visualisation.		15. NUMBER OF PAGES 93	
		16. PRICE CODE	
17. SECURITY CLASSIFICATION OF REPORT Unclassified	18. SECURITY CLASSIFICATION OF THIS PAGE Unclassified	19. SECURITY CLASSIFICATION OF ABSTRACT Unclassified	20. LIMITATION OF ABSTRACT UL

Approved for public release; distribution is unlimited

## DEEP CONVECTION IN THE MEDITERRANEAN SEA

by

Bernard Arata

Lieutenant, French Navy

B.S., French Naval Academy, 1983

Submitted in partial fulfillment of the  
requirements for the degree of

## MASTER OF SCIENCE IN PHYSICAL OCEANOGRAPHY

from the

NAVAL POSTGRADUATE SCHOOL

September 1994

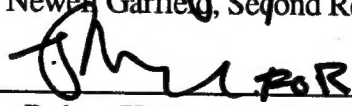
Author: \_\_\_\_\_

  
Bernard Arata

Approved by: \_\_\_\_\_

  
Roland W. Garwood, Jr., Thesis Advisor

  
Newell Garfield, Second Reader

  
Robert H. Bourke, Chairman  
Department of Oceanography

Accession For		
NTIS	CRA&I	<input checked="checked" type="checkbox"/>
DTIC	TAB	<input type="checkbox"/>
Unannounced		<input type="checkbox"/>
Justification		
By _____		
Distribution /		
Availability Codes		
Dist	Availability Codes	
A-1		

## ABSTRACT

It is now understood that deep convection in the ocean plays a dominant role in determining the climate of the world's oceans. Recent theoretical advances in explaining oceanic convection need to be tested by real observations. Satellite observations of deep convection regions may be a promising new tool in studying this phenomenon. This thesis examines deep convection events in two ways:

- To assess the characteristic elements of a deep convection event using two different prediction models based upon the turbulent kinetic energy budget.
- To attempt to observe deep convection phenomena signals in altimeter data.

In 1987, a deep convection event was observed in the northwestern Mediterranean sea (Schott and Leaman 1991). These data, combined with GEOSAT altimeter data, were used to verify the Kraus and Turner and the Naval Postgraduate School mixed layer model predictions of the time evolution of temperature, salinity and mixed layer depth. Both models predicted final values similar to the observations, but model tuning was required to reproduce the observed rapid mixed-layer deepening. The interpolated altimeter field does not allow identification with confidence of the Mediterranean convection area. However, a locally persistent feature and the mean winter sea surface topography field agree with in-situ observations and do provide some indication about where and when the convection process occurs.

## TABLE OF CONTENTS

I. INTRODUCTION .....	1
II. THE CONVECTION PROCESS IN THE MEDITERRANEAN SEA .....	3
A. A THREE-PHASE PROCESS .....	3
B. DEEP CONVECTION MECHANISMS AND MODELS .....	5
C. THE RESULTS OF THE MEDOC EXPERIMENT .....	5
III. ASSESSMENT OF CHARACTERISTIC DEEP CONVECTION ELEMENTS USING TWO SIMPLE MODELS .....	9
A. THE GOVERNING SET OF EQUATIONS .....	9
1. Zones of the water column .....	9
2. The temperature and salinity equations .....	10
3. The turbulent kinetic equation .....	12
B. THE KRAUS AND TURNER CLOSURE (1967) .....	12
C. THE KRAUS AND TURNER SIMULATION .....	13
1. Initialization of the simulation .....	13
2. Constant coefficients simulation .....	16
a. Constant atmospheric forcing .....	16
b. Variable atmospheric forcing .....	16
c. Comparison to in-situ profiles .....	17
3. Variable coefficients simulation .....	19
a. Heat flux forcing alone ( $c_1=0$ ) .....	20
b. Wind forcing alone ( $c_2=0$ ) .....	20
c. Adjustment of the tuning coefficients .....	20
D. THE NAVAL POSTGRADUATE SCHOOL CLOSURE .....	21
1. The NPS mixed layer model equations .....	21

2. Special functions and constants .....	23
3. Role of each coefficients .....	24
E. THE NPS SIMULATION .....	25
1. Simulation under normal conditions .....	25
a. Constant atmospheric forcing .....	25
b. Variable atmospheric forcing .....	25
2. Role of the Coriolis parameter .....	26
3. The influence of the M coefficients .....	26
a. Search for the best coefficients .....	26
b. A NPS simulation with deep convection coefficients .....	27
c. Validity of the coefficients found .....	28
F. SUMMARY OF THE SIMULATIONS .....	29
G. PARTIAL CONCLUSION AND RECOMMENDATIONS .....	30
IV. REMOTE SENSING AND DEEP CONVECTION .....	41
A. MOTIVATION .....	41
1. Previous work on the subject .....	41
2. Theoretical computation of the observable signal .....	42
B. THE GEOSAT ALTIMETER .....	43
1. The geodesy satellite .....	43
2. The principle of the altimeter measurement .....	43
3. The altimeter characteristics .....	44
4. Typical altimeter problems .....	44
C. DATA ANALYSIS .....	45
1. The altimeter data .....	45
2. The corrections applied to the data .....	45

3. Delimitation of the study and plan of investigation .....	46
4. Producing monthly interpolated frames .....	48
a. Monthly mean frames .....	48
b. The interpolation process .....	49
c. Searching the best interpolation coefficients .....	51
D. RESULTS .....	52
1. The averaged heights .....	52
a. Interpretation of the results .....	52
b. Comparison to in-situ observations .....	53
2. The smoothed tracks .....	53
3. The averaged winter frame .....	53
E. PARTIAL CONCLUSION AND RECOMMENDATIONS .....	54
V. CONCLUSION .....	67
LIST OF REFERENCES .....	69
INITIAL DISTRIBUTION LIST .....	73

## LIST OF FIGURES

1. Bathymetry of the Golfe du Lion, in Northwestern Mediterranean Sea and the Locations of the CTD and PEGASUS Stations and the ADCP Moorings during the 1987 Mediterranean Convection Experiment From Leaman and Schott 1991.....	3
2. Schematic of a Deep Convection Process. Evolution of the Density Profile.....	4
3. Time Series of Vertical Component of the Current at 375 meters in February 1987.....	6
4. Typical Temperature Profile in a Water Column.....	9
5. Digitalized Temperature, Salinity and Density Profile at the Beginning of the Deep Convection Event.....	14
6. Total Heat Flux and Windstress vs. Time during the Deep Convection Event. After Leaman and Schott 1991.....	15
7. In-situ Temperature, Salinity and Density Profiles after the Deep Convection Event. From Schott and Leaman 1991.....	16
8. Potential Temperature at 537 Meters during the Convection Event.....	17
9. KT Simulated Temperature at 530 Meters during the Convection Event.....	18
10. Reconstituted NPS Temperature at 530 Meters with Deep Convection Coefficients...	28
11. Kraus and Turner Simulation of the Variation of Mixed Layer Depth, Temperature, Salinity and Density with Time under Constant Windstress and Heat Flux.....	31
12. Kraus and Turner Simulation of the Variation of Mixed Layer Depth, Temperature, Salinity and Density with Time under Actual Windstress and Heat Flux.....	32
13. Kraus and Turner Simulation of the Variation of Mixed Layer Depth, Temperature, Salinity and Density with Time under Actual Windstress (----) or Heat Flux (-.-.-).....	33
14. Kraus and Turner Simulation of the Variation of Mixed Layer Depth, Temperature, Salinity and Density with Time under Actual Windstress and Heat Flux using Adjusted Coefficients ( $c_1=1, c_2=2$ (.....) / $c_1=2, c_2=1$ (-.-.-) / $c_1=2, c_2=2$ (----) ).....	34
15. Naval Postgraduate School Simulation of the Variation of Mixed Layer Depth, Temperature, Salinity and Density with Time under Constant Windstress and Heat Flux.....	35



16. Naval Postgraduate School Simulation of the Variation of Mixed Layer Depth, Temperature, Salinity and Density with Time under Actual Windstress and Heat Flux.....	36
17. Naval Postgraduate School Simulation of the Variation of Mixed Layer Depth, Temperature, Salinity and Density with Time under Actual Windstress and Heat Flux and No Rotation.....	37
18. Search for the Best Set of Coefficients. Naval Postgraduate School Simulation of the Variation of Mixed Layer Depth and Temperature with Time under Actual Windstress and Heat Flux using Different Sets of Coefficients.....	38
19. Naval Postgraduate School Simulation of the Variation of Mixed Layer Depth, Temperature, Salinity and Density with Time under Actual Forcing using Different Coefficients.....	39
20. Time Series of Mean In-situ Turbulent Kinetic Energy at 450 meters and Turbulent Kinetic Energy Produced by the Naval Postgraduate School Model under Actual Forcing using Different Coefficients.....	40
21. The Altimeter Measurement System. From John Hopkins APL 1987.....	44
22. The Area of Investigation and the GEOSAT Ground Tracks Used.....	47
23. The Principle of Averaging Two Collinear Tracks.....	49
24. The Residual Heights after the Two Year Mean and Bias Removal.....	55
25. The Residual Height of Track 487 after the Two Year Mean and Bias Removal.....	56
26. The Influence of the Multiquadric Interpolation Parameters on the Interpolated Field .....	57
27. Monthly Frames (November 1986 - July 1987) of Interpolated Field Produced with Averaged Heights.....	58
28. Monthly Frames (August 1987 - April 1988) of Interpolated Field Produced with Averaged Heights.....	59
29. Zoom of the Convection Area of Monthly Frames (November 1986 - July 1987) of Interpolated Field Produced with Averaged Heights.....	60
30. Same as Fig. 29 but for the Period November 1986 - February 1987.....	61

31. Time Series of the Track 487 (November 1986 - February 1987).....	62
32. The Deep Mixed Path inside the Convection Area during the Convection Period. From Leaman and Schott 1991.....	63
33. Monthly Frames (November 1986 - July 1987) of Interpolated Field Produced with Smoothed Heights.....	64
34. Sea Surface Density in Winter from Historical Data. From Madec et al. 1991.....	65
35. Mean Winter Interpolated Altimeter Field.....	66

## **ACKNOWLEDGMENT**

I would like to thank Dr. Friedrich Schott for providing data from the 1987 Mediterranean convection experiment and Dr. Robin Tokmakian for the GEOSAT data as well as some programs needed for their exploitation.

The interpolation program was developed by LT Rogerio Chumbinho and I would like to offer my appreciation for the use of his program.

## I. INTRODUCTION

It is now recognized that deep convection to depths exceeding about one kilometer occurs in very few areas in the world's oceans. Locations of deep convection are mostly limited to polar regions such as the Labrador, Weddell, and Greenland seas. However, deep convection also occurs in the Northwestern Mediterranean sea. The process of deep convection is very important in deep-water formation and thus plays a fundamental role in determining the climate of the world's oceans.

Deep convection in the open sea has been studied for more than twenty years. Observations and models are now available. These models have helped explain the phenomenon on a global scale, but not the small scale. Recent theoretical advances have been made (Garwood 1991; Garwood et al. 1994; Paluszkievicz et al. 1994) and need to be tested by real observations. Satellite observations of deep convection regions have rarely been analyzed and the large variety of remote sensing instruments may open promising new ways to study this phenomenon.

The 1987 Mediterranean convection experiment (Schott and Leaman 1991; Leaman and Schott 1991) documented a deep convection event in the Golfe du Lion. Data were recorded between January 25 and March 6. Altimeter data from GEOSAT for the same period and location, but independent from the experiment, were also used in this study.

The purpose of this thesis is examine a Mediterranean deep convection event in two ways:

- To assess the characteristic elements of a deep convection event using two one-dimensional models based upon the turbulent kinetic energy (TKE) budget.
- To look at deep convection phenomena using remote sensing instruments.

The Kraus and Turner (1967) model and the Naval Postgraduate School model (Garwood 1977; 1991) with realistic forcing and initial conditions, will be used to predict the evolution of temperature, salinity, TKE and mixed layer depth with time and to

compare them with in-situ profiles. An analysis of the satellite data will be conducted to identify sea level changes in time and space, thus potentially being able to remotely identify the deep convection process.

## II. THE CONVECTION PROCESS IN THE MEDITERRANEAN SEA

### A. A THREE-PHASE PROCESS

A few areas in the world ocean have been identified as locations of winter deep convection (Killworth 1976). Along with the Labrador, Weddell and Greenland seas, the northwestern Mediterranean Sea, especially the Golfe du Lion south of France, is also a convection-favorable region. Due to easy access and often predictable triggering factors, the deep convection and the formation of deep water in the Golfe du Lion have been the subject of a few observational studies and modeling. From 1969 (Medoc group 1970) to the 1987 experiment (Schott and Leaman 1991, Leaman and Schott 1991), deep convection has been observed many times, each time improving the understanding of the "pre-conditioning" phase, the "violent mixing" phase and the "sinking and spreading" phase (Medoc group 1970) of deep convection (Fig. 2).

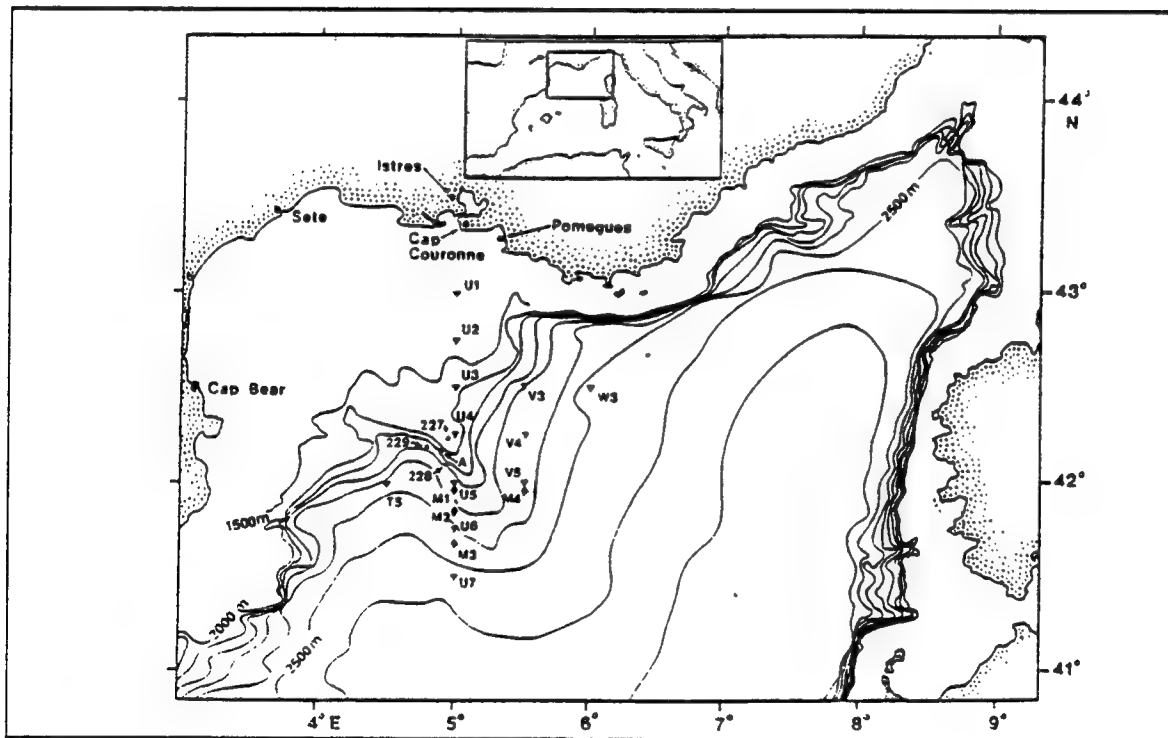


Figure 1. Bathymetry of the Golfe du Lion, in Northwestern Mediterranean Sea and the Locations of the CTD and PEGASUS Stations and the ADCP Moorings during the 1987 Mediterranean Convection Experiment From Leaman and Schott 1991.

The pre-conditioning phase is characterized by three favorable factors (Fig.1; Schott and Leaman 1991). Firstly, the wintertime cyclonic circulation induces a doming of the isopycnals in its center causing the typical Mediterranean three-layer stratification to have a noticeably weaker stratification below the surface layer (Swallow and Gaston 1973). The second factor is the conelike topography of the Rhone fan (42°N-5°E), which may induce cyclonic circulation with a predictable position for the center of the dome each winter (Hogg 1973). The last factor is the incidence of two cold and dry winds, originating from the continent and directed toward the center of the dome: Mistral from the Rhone Valley and Tramontane from the Pyrenees. Cooling and evaporation are increased by these winds which act to destabilize the oceanic upper layer (phase 1 in Fig. 2). Once this convective instability occurs, the preconditioning phase is followed by vertical convection associated with large downward vertical velocities (Fig. 3) which penetrate to deep levels since the pre-existing stratification below the surface is weak. During the last phase, the new deep water spreads away from the formation area.

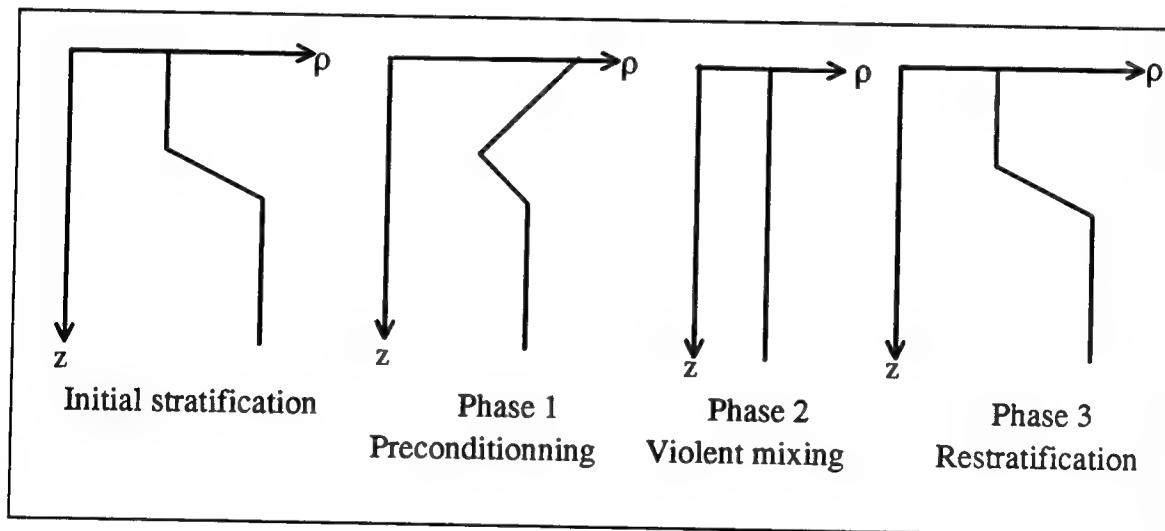


Figure 2. Schematic of a Deep Convection Process: Evolution of the Density Profile.

## **B. DEEP CONVECTION MECHANISMS AND MODELS**

The mechanisms responsible for the establishment of the mixed water column have been the subject of numerous investigations. The mechanisms proposed include gravity-inertial waves (Gascard 1973), convective process with baroclinic adjustment (Gascard 1978), comparison to atmospheric thermals (Vaughan 1993) or parcel instability mechanism (Garwood 1991), taking into account "thermobaricity" (increase of the thermal expansion coefficient with pressure). A few models have been developed to predict what the MEDOC group in 1970 characterized as a homogeneous column of water created by vertical mixing due to strong surface cooling. Killworth (1976) used a two-dimensional model where the violent mixing phase was explained by one dimensional non-penetrative convection coupled with geostrophic adjustment. A multilevel numerical model (Madec et al. 1991) of the Laboratoire d'Océanographie Dynamique et de Climatologie (LODYC) used the mechanism proposed by Gascard (1978).

## **C. THE RESULTS OF THE MEDOC EXPERIMENT**

Medoc 69 (Medoc group 1970) and the experiment of the winter of 1987 (Schott and Leaman 1991, Leaman and Schott 1991) provide the most extensive observations of convection in the Northwestern Mediterranean Sea. In 1969, a large (20 km x 50 km) and deep (1500-2000 m) well-mixed region was observed over the Rhone fan. The vertical velocities, measured by neutrally buoyant rotating floats, showed upward and downward velocities  $O(2-3 \text{ cm/s})$ . The existence of rotating plumes  $O(6 \text{ km diameter})$  was also deduced (Voorhis and Webb 1970).

Using Acoustic Doppler Current Profilers (ADCP), Vector Averaging Current Meters (VACM), Conductivity Temperature and Depth instruments (CTD) on site and coastal meteorological measurements, the 1987 experiment collected numerous data. ADCP measures currents in three dimensions over a fairly large range with an accuracy and time resolution allowing measurements of vertical velocities during convective events. An array of three moorings with upward-looking ADCP on top was deployed in the Golfe



du Lion between January 24 and March 6. Unfortunately, a strong Mistral had already occurred in early January and triggered the convective process. A second convective event took place between February 12-22 and was fully recorded.

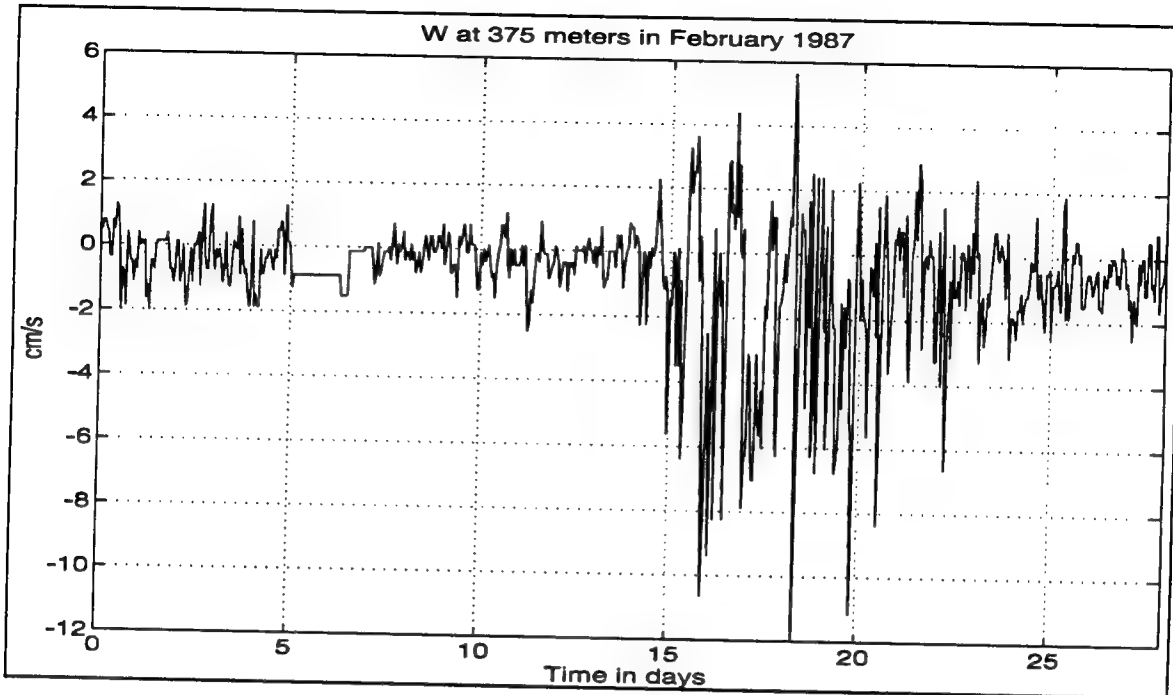


Figure 3. Time Series of Vertical Component of the Current at 375 meters in February 1987.

The time series of the vertical current in Fig. 3 shows large downward velocities up to 10 cm/s associated with the second Mistral period in mid February 1987. There was almost no change in the velocity records with depth, confirming that the violent mixing phase is very swift and occurs throughout all the water column. The variability of the vertical kinetic energy observed during the calm and the windy periods tends to refute the internal wave, mechanical wind or wave forcing theories. This variability is associated with convection following surface cooling (Schott and Leaman 1991). Based on the assumptions that (1) the downward velocity events are quasi-stationary at the time scale of the observations (one hour) and (2) that the background flow is homogeneous, a diameter of

1 kilometer can be deduced for the convection cells (Schott and Leaman 1991). They are embedded in the convective area itself  $O(100 \text{ km})$  from which eddies  $O(5 \text{ km})$  detached (Gascard 1978). Other interesting results concern the surface circulation and the movement of the lighter surface water between Mistral events. A correlation was also found between deep water temperature changes and the magnitude of surface cooling. Finally, gravitationally unstable surface layers were observed during periods of heightened atmospheric forcing.

### III. ASSESSMENT OF CHARACTERISTIC DEEP CONVECTION ELEMENTS USING TWO SIMPLE MODELS

In this chapter the characteristic elements of a deep convection process are assessed. The Kraus and Turner model and the Naval Postgraduate School model will be used to evaluate the deepening and the evolution of temperature, salinity and density of the mixed layer during that phenomenon. Both models will be initiated with real data and the results of the runs will be compared to the observed profiles. The Kraus and Turner (KT) model and the Naval Postgraduate School (NPS) model are both one-dimensional models based on the vertically integrated turbulent kinetic energy (TKE) equation. They differ by the way some of the terms of the TKE budget are modeled or neglected, the KT model being the simpler of the two.

#### A. THE GOVERNING SET OF EQUATIONS

##### 1. Zones of the water column

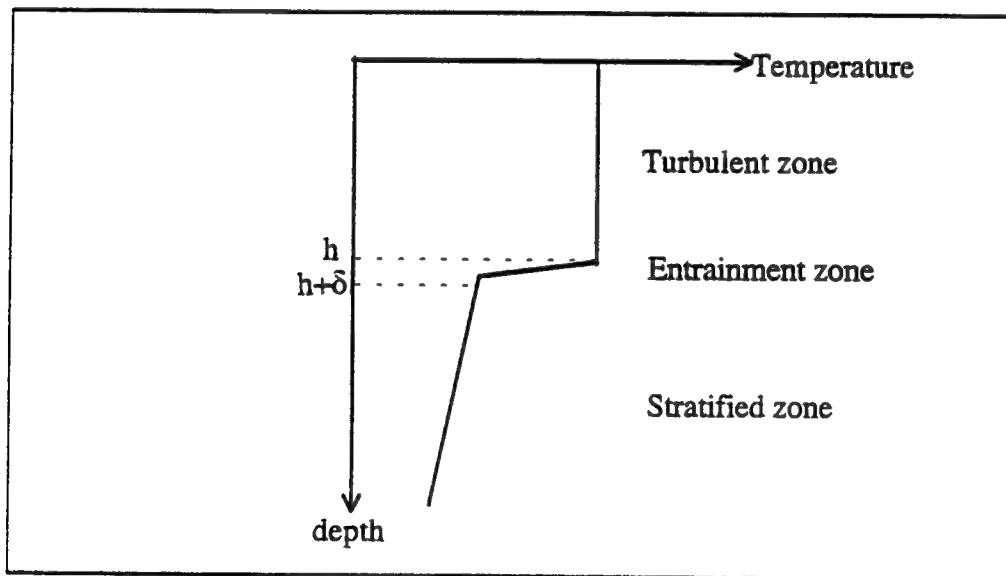


Figure 4. Typical Temperature Profile in a Water Column.

The following equations refer to a typical water column which can be divided into three regions as seen on Fig. 4:

- From the surface to depth  $h$ , the well mixed layer is where the temperature and salinity are constant due to strong turbulent mixing.
- The interface region between  $h$  and  $h+\delta$ , is a region of sharp temperature and salinity gradient also called entrainment region.
- The turbulence free or stratified zone is where the temperature decreases with depth.

## 2. The temperature and salinity equations

The equation of conservation of mean temperature with the assumption of horizontal homogeneity (vertical gradients much larger than the horizontal gradients), yields:

$$\frac{\partial \bar{T}}{\partial t} + \bar{W} \frac{\partial \bar{T}}{\partial z} + \frac{\partial}{\partial t} (\overline{T'w'}) = 0 \quad (3.1)$$

We first integrate Eq. 3.1 with respect to  $z$  over the mixed layer depth (MLD)  $h$ . There is no advective term because  $T$  is constant in the mixed layer, and we use the assumption that the entrainment zone thickness  $\delta \ll h$ . Knowing that the surface heat flux can be rewritten using the total heat flux  $Q_0$ , the density  $\rho$  and a heat coefficient  $C_p$ :

$$\overline{w'T'}(0) = \frac{Q_0}{\rho C_p} \quad (3.2)$$

the combination of Eq. 3.1 vertically integrated and Eq. 3.2 gives a prediction equation for the mean temperature in the mixed layer:

$$\frac{\partial \bar{T}}{\partial t} = \frac{Q_0}{\rho C_p h} - \frac{\overline{w'T'}_{-h}}{h} \quad (3.3)$$

In a similar manner, we have an equation for the mean mixed layer salinity:

$$\frac{\partial \bar{S}}{\partial t} = \frac{S(e-p)}{h} - \frac{\overline{w' S'}}{h} \quad (3.4)$$

where  $(e-p)$  is the net evaporation minus precipitation.

The rate of mixed layer deepening with time is obtained by integrating Eq. 3.1 across the interface. Since the interface is moving, we have to use the Liebniz rule,

$$\int_{a(t)}^{b(t)} \frac{\partial F}{\partial t} dz = \frac{\partial}{\partial t} \int_{a(t)}^{b(t)} F dz + F[z = a(t)] \frac{\partial a(t)}{\partial t} - F[z = b(t)] \frac{\partial b(t)}{\partial t} \quad (3.5)$$

Using  $F = \bar{T}$  and limits such that  $a(t) = h(t)$  and  $b(t) = h(t) + \delta$ , this integration gives the "jump condition" which relates the entrainment velocity to the temperature jump at the base of the mixed layer and the heat flux across the interface,

$$w_e = \frac{\partial h}{\partial t} + \bar{w}_{-h} = -\frac{\overline{w' T'}}{\Delta T} \quad \text{or} \quad \frac{\partial h}{\partial t} = w_e - \bar{w}_{-h} \quad (3.6)$$

This means that  $h$  can be changed by entrainment and upwelling or downwelling.

A jump condition can be also written for the salinity :

$$w_e = -\frac{\overline{w' S'}}{\Delta S} \quad (3.7)$$

We shall assume here that there is no up/downwelling so that the change with time of the mixed layer depth is only due to entrainment.

The combination of Eq. 3.3, Eq. 3.4, Eq. 3.6 and Eq. 3.7 gives new prediction equations for the mean mixed layer temperature (3.8) and salinity (3.9).

$$\frac{\partial \bar{T}}{\partial t} = \frac{Q_o}{\rho \cdot C_p \cdot h} - \frac{\Delta T}{h} \frac{\partial h}{\partial t} \quad (3.8)$$

$$\frac{\partial \bar{S}}{\partial t} = \frac{S(e-p)}{h} - \frac{\Delta \bar{S} \cdot w_e}{h} \quad (3.9)$$

This equation for the mean sea surface temperature simply indicates that both surface heating/cooling and entrainment mixing will change the mean temperature in the mixed layer.

### 3. The turbulent kinetic equation

Our system is now composed of two equations (Eq. 3.8 and Eq. 3.9) and three unknowns:  $\bar{T}$ ,  $\bar{S}$  and  $h$  or  $w_e = \frac{\partial h}{\partial t}$ . To solve it, we need another equation which will be provided by the turbulent kinetic energy (TKE) equation:

$$\frac{\partial}{\partial t} \left( \frac{\overline{u'^2 + v'^2 + w'^2}}{2} \right) = \underbrace{(-\overline{u'w'} \frac{\partial \bar{u}}{\partial z} - \overline{v'w'} \frac{\partial \bar{v}}{\partial z})}_{\text{shear production}} + \underbrace{\left( \frac{\overline{p'w'}}{\rho_o} g \right)}_{\text{buoyancy flux}} - \underbrace{\frac{\partial}{\partial z} \left( \overline{w' \left( \frac{u'^2 + v'^2 + w'^2}{2} + \frac{p'}{\rho_o} \right)} \right)}_{\text{turbulent transport}} - \epsilon \quad (3.10)$$

storage                      shear                      buoyancy                      turbulent transport                      dissipation

There is assumed to be no turbulence below the base of the mixed layer.

## B. THE KRAUS AND TURNER CLOSURE (1967)

Kraus and Turner used the TKE budget with the following assumptions to derive the third equation:

- The pressure redistribution in the turbulent transport term is neglected.
- The dissipation is included in the shear production and buoyancy flux through the tuning coefficients ( $c_1$  and  $c_2$ ).
- A steady state is assumed.

The equation of state is used to express the buoyancy flux in terms of heat and salinity fluxes.

$$\rho \cong \rho_o [1 - \alpha(T - T_o) + \beta(S - S_o)] \quad (3.11)$$

With these assumptions, the vertical integration of the TKE equation reduces to :

$$c_1 \frac{u^{*3}}{h} - c_2 [\alpha g (\frac{Q_o}{\rho C_p}) + \beta g S(e-p)] - (\alpha g \Delta T - \beta g \Delta S) \frac{\partial h}{\partial t} = 0 \quad (3.12)$$

The integrated transport of TKE averaged over the mixed layer is zero because there is no external source or sink for turbulence. This equation gives the entrainment velocity or rate of deepening in terms of wind stress, heat and salinity fluxes and temperature and salinity jumps at the base of the mixed layer.

For our purpose we will assume that the contribution of the salinity term is much smaller than the heat flux term. This can be proven by a quick computation. The excess of evaporation over precipitation in Mediterranean sea can be estimated to 1 meter per year (Pickard et al. 1990). Thus the salinity term in Eq. 3.12 has an order of magnitude of  $400 \text{ m}^2/\text{h}^3$  whereas the heat flux term has a mean value of  $4000 \text{ m}^2/\text{h}^3$  during the convection period. This ratio of 10 is enough to neglect the salinity contribution.

Equations 3.8, 3.9 and 3.12 are now used in a Matlab program to evaluate the evolution of the depth, temperature and salinity of the mixed layer with time.

## C. THE KRAUS AND TURNER SIMULATION

### 1. Initialization of the simulation

The Kraus and Turner model is simple and easy to program. The input variables are the initial potential temperature and salinity profiles, the total heat flux, the friction velocity and the tuning coefficients.

Two series of simulations will be examined. First, both coefficients will be set to unity to give an equal contribution by the wind and heat flux. We will examine cases with both constant and variable atmospheric forcing. Then under a variable forcing, we will adjust the coefficients to try to reproduce the Mediterranean convection event.

The program runs for ten days with digitalized observations for initial temperature and salinity profiles (Fig. 5) and real forcing (Fig. 6). Notice that the strong unstable

temperature profile is balanced by a strong stable salinity profile to produce a typical Mediterranean winter profile (stable-neutral at the surface / strongly stable for the intermediate layer / neutral for the deep layer).

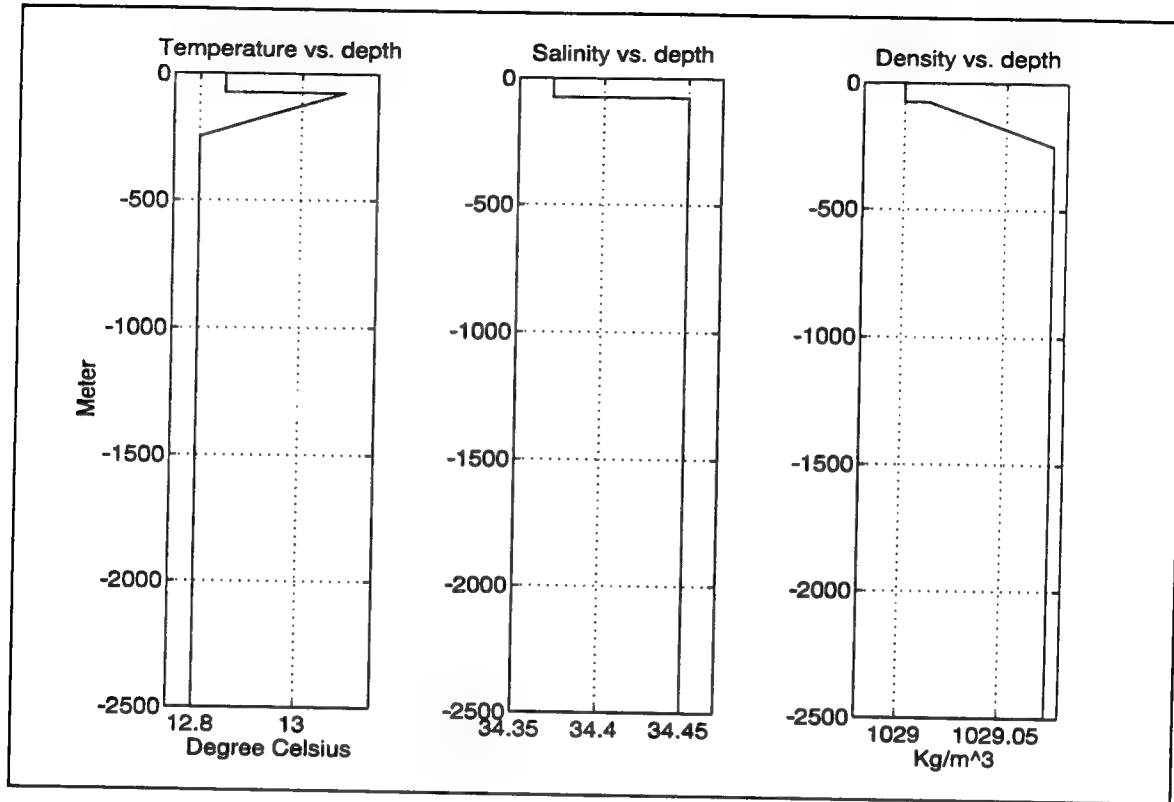


Figure 5. Digitalized Temperature, Salinity and Density Profiles at the Beginning of the Deep Convection Event

This ten day period corresponds to the Mediterranean deep convection event observed in February 1987 (Schott and Leaman 1991; Leaman and Schott 1991). The period was delimited by examining the period of strong atmospheric forcing (February 12 - 22) that corresponds to the period of maximum downward velocity as well as homogenization of the water column.



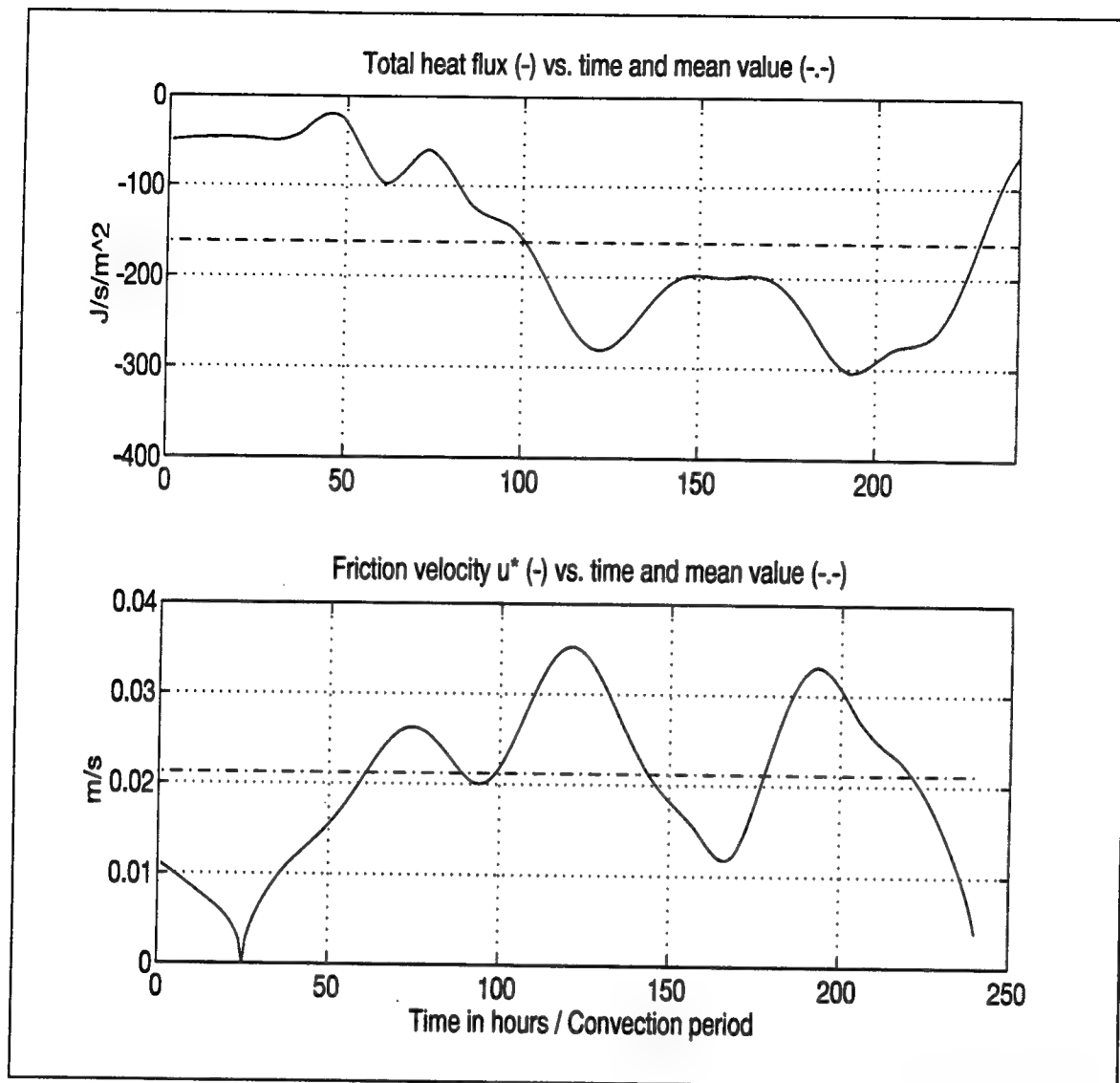


Figure 6. Total Heat Flux and Windstress vs. Time during the Deep Convection Event. After Leaman and Schott 1991.

The Matlab function ode45 was used to integrate the system of ordinary differential equations using 4th and 5th order Runge-Kutta formula.

The results of the different runs are discussed in the following section, the plots are presented at the end of the chapter.

## **2. Constant coefficients simulation**

### ***a. Constant atmospheric forcing***

The constant values used as input for the atmospheric forcing are the means of the total heat flux and friction velocity over the ten-day convective period. The mixed layer deepens to 950 meters after ten days as shown on Fig. 11. There is an inflection point around hour 75 that indicates an extrema in the slope of the curve, thus a change in the rate of deepening. Since the forcing is constant, the change is linked to the change in temperature and salinity profiles at 250 meters.

The mixed layer temperature shows an early peak that can be explained by the mixing of the intermediate warm water with the colder surface water. This mixing also takes 75 hours to complete. When the mixed layer is then homogenized, the situation becomes similar to the classical two-layer mixing case in which warm water overlays cold water. The temperature decreases uniformly to 12.79°C. Meanwhile, the mixed layer salinity steadily increases, which is normal when mixing the initial profile. The density profile shows no significant change during the period.

### ***b. Variable atmospheric forcing***

Allowing the wind stress and total heat flux to change with time (Fig. 12) produces its most visible effect on the mixed layer depth. The depth reached after ten days is now 1150 meters. The curves are not as smoothed as in the previous plots and reflect somewhat the variations in the forcing. However, the global shape of all curves is preserved.

During the first 50 hours, the forcing is weak, thus the curves show a slow departure from the initial conditions. Since the deepening is slower, the mixing with the warmer and saltier intermediate water takes more time with peak temperature at 80 hours instead of 20 hours. On the other hand, the values of more intense surface forcing found around hour 200 induce a rapid increase in the mixed layer depth. At that time, the temperature and salinity have already reached their final values and show no further evolution.

### c. Comparison to in-situ profiles

The in-situ deep convection temperature and salinity profiles of Fig. 7 (Leaman and Schott 1991) show a rapid homogenization of the layer. Within a few hours to half a day, the stratification has totally disappeared, and the profiles are simply straight lines. This also underlines the importance of the preconditioning phase. The water column is so well prepared that the weak forcing at the beginning of the period (February 13) can trigger the deep convection process.

In our simulation, the KT model deepens the layer to the bottom in more than ten days. The maximum depth reached was 1200 meters with a bottom depth of 2500 meters. However, the final mixed layer temperature and salinity (12.79°C and 38.445) agree fairly well with the temperature and salinity found in the water column immediately after the convection event (12.81°C and 38.45; Fig. 7).

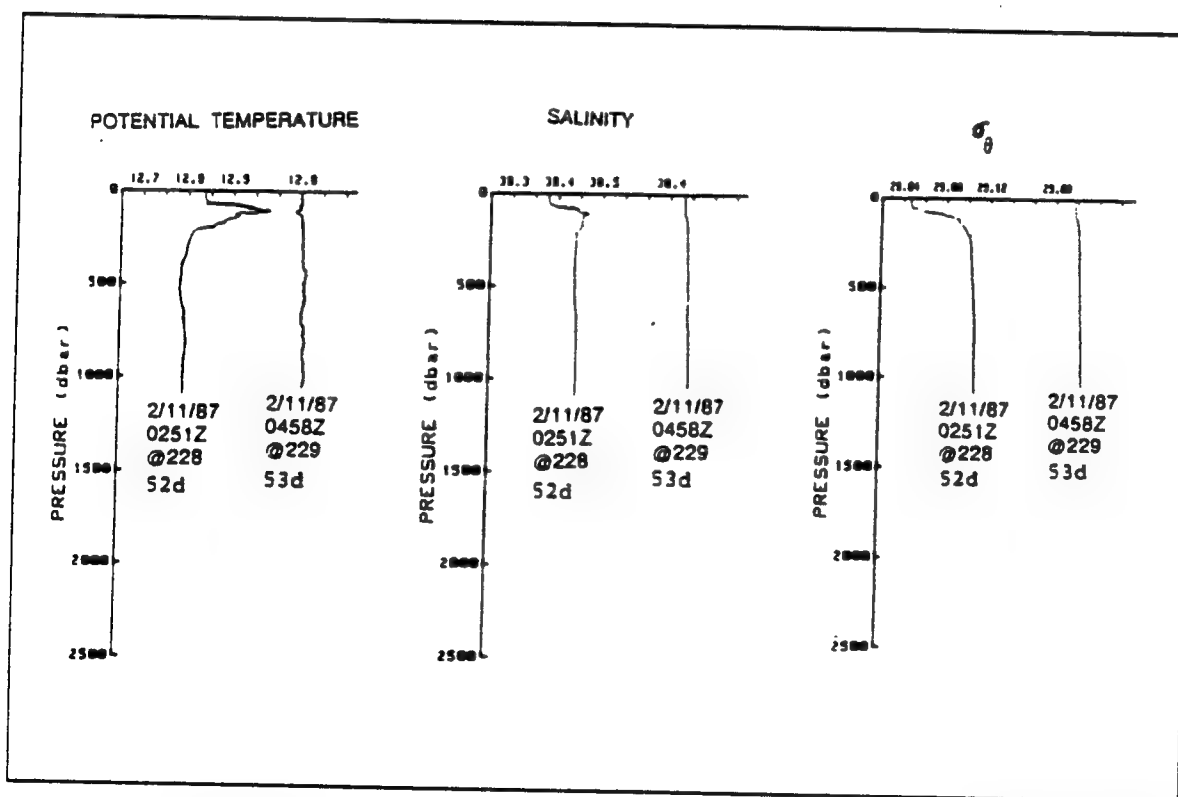


Figure 7. In-situ Potential Temperature, Salinity and Sigma Theta Profiles before and after a Deep Convection Event. From Leaman and Schott 1991.

The temperature recorded at 537 meters during the convection has been averaged over six hours and is presented in Fig. 8, along with the original recording. This measurement can be assimilated to an Eulerian observation. The time series goes further in time than the profiles of Fig. 7. Some gaps in the data recording are present but small time scale variations are evident while the temperature decreases slightly. Although the variations are very small and must be analyzed carefully, this indicates that the convection process is not a simple event in time but a sum of short time scale events and/or that even when the water column seems homogenized, there is still turbulent mixing occurring.

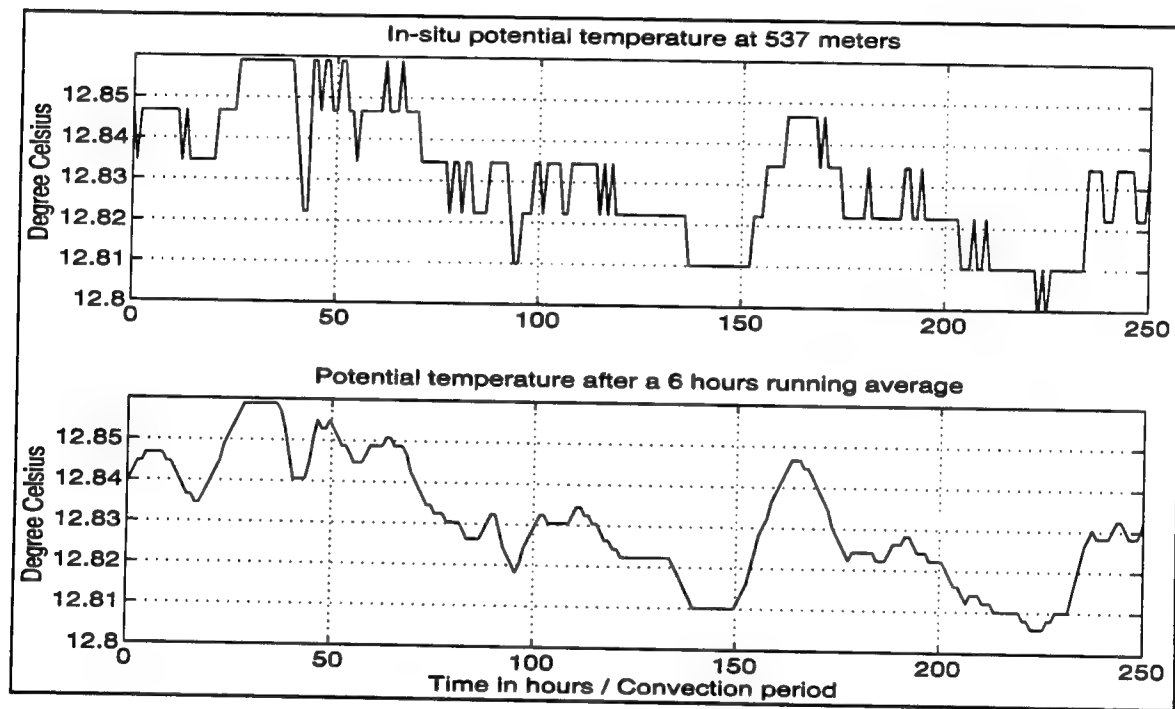


Figure 8. Potential Temperature at 537 Meters during the Convection Event

On the contrary, the simulated temperature is the mean temperature above the interface, the time series represents the temperature evolution as the interface deepens. It is a Lagrangian measurement. The KT physics do not account for subsequent cooling that would modify the upper layer and create a new colder and sinking water mass.

The Fig. 9 is what a sensor at 530 meters would see, using the information we know about temperature and depth from the KT simulation.

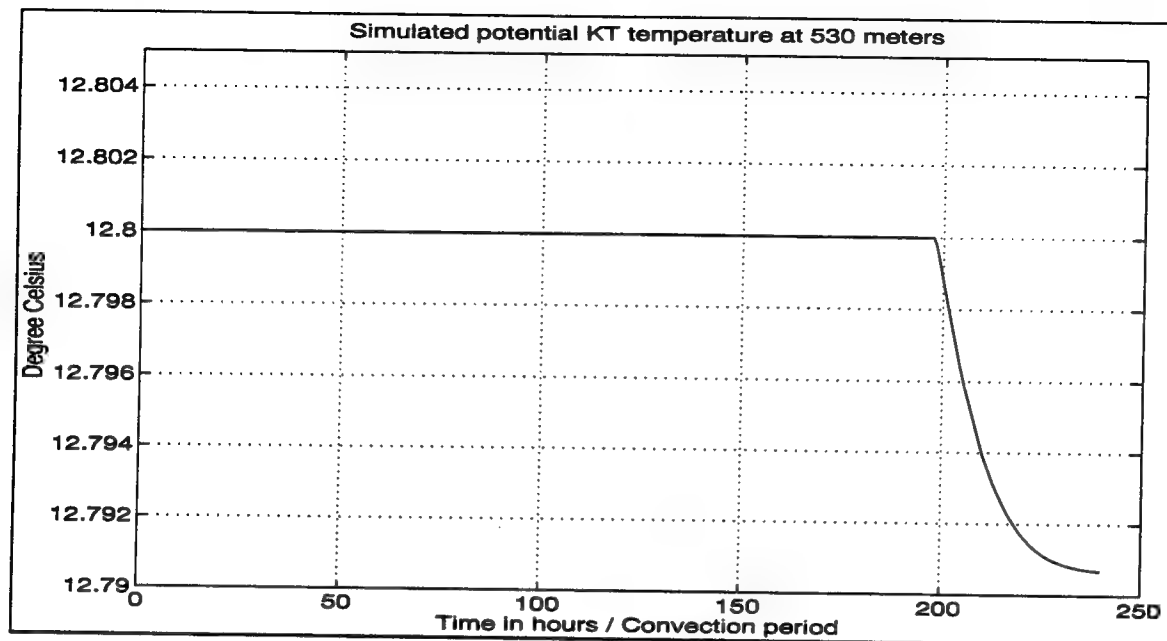


Figure 9. Simulated Temperature at 530 meters during the Convection Event

Unfortunately, there is no possible comparison. The simulated temperature evolves only after the interface has reached the level of 530 meters, almost at the end of the convection period. This reveals some of the limitations of this model; successive coolings and the rapidity of the process cannot be modeled.

This model extends the process of deep convection over a longer period than found in reality. The final results are consistent with the real case and are reasonable considering the simplicity of the model.

### 3. Variable coefficients simulation

Simple cases such as  $c1=0$  (heat flux forcing only) or  $c2=0$  (wind stress forcing only) will allow the assessment of the respective roles of the wind stress and heat flux in the deepening of the mixed layer. Then we will double the coefficients one at a time, and

finally all together. Since we are using a relatively simple model, our aim is to have the mixed layer depth reach the bottom by the end of the period of strong surface forcing.

***a. Heat flux forcing alone ( $c1=0$ )***

The deepening due to surface cooling alone leads to a mixed layer depth of 650 meters (dot dashed plots in Fig. 13). The first two days of weak heat flux are evident in all the plots: the rate of deepening is zero and there is no evolution in either the temperature or the salinity. When the heat flux increases it triggers the mixing, producing profiles similar to those found in the previous cases. The changes in the deepening rate correspond to the variations in the heat flux forcing at hours 100 and 175. Beside the mixed layer depth, all the final values are consistent with the observed ones.

***b. Wind forcing alone ( $c2=0$ )***

In the KT simulation, the wind (solid plots in Fig. 13) doesn't seem to be sufficiently powerful to mix to a deep level. The mixed layer depth reaches 275 meters. The wind was significant during that period (10 to 20 m/s), and its variations can easily be seen in all the curves. Since the rate of the mixing is slowed, the peak and final temperatures are both slightly higher than for the previous runs (12.915°C and 12.888°C, respectively). For the same reason, the salinity and density profiles show lower final values.

Therefore, in the variable atmospheric forcing, the heat flux forcing is the dominant mechanism responsible for the mixing.

***c. Adjustment of the tuning coefficients***

The adjustment is based on the variation of the mixed layer depth in time. The temperature, salinity and density profiles are similar for the three following runs; they show exactly the same shape as for the constant coefficients section and reach the observed values after ten days.

- Experiment #1:  $c1=1$  /  $c2=2$ : We have already shown that the heat flux was the dominant process of the mixing. Thus by increasing its coefficient, the bottom is reached sooner (dotted plots in Fig. 14).

- Experiment #2:  $c1=2 / c2=1$ : The result is not very different from the original variable atmospheric forcing case with both coefficients set to unity. Again, this tells us that the influence of the wind stress is weak (dot dashed plots in Fig. 14).
- Experiment #3:  $c1=2 / c2=2$ : It is the combination of the two previous experiments. The bottom is reached at time 215 hours (solid plots in Fig 14).

This set of tuning experiments proves that the bottom can be reached with a KT simulation. This is easily done by doubling the  $c2$  coefficient, increasing the heat flux influence. This may also signify that in a deep convection process the heat flux largely dominates the wind stress, however strong it is.

#### D. THE NAVAL POSTGRADUATE SCHOOL CLOSURE

The Naval Postgraduate School mixed layer model (Garwood 1977) is a one-dimensional model using a bulk second-order turbulence closure system for closure using TKE equation. This model differs from the Kraus and Turner model in five ways:

- Three equations now describe the TKE budget (one for each component  $u'^2$ ,  $v'^2$  and  $w'^2$ ).
- The dissipation is equally distributed into the three parts of the TKE equation ( $D/3$  for each equation; this is a good approximation for turbulent flow).
- The pressure redistribution is modeled ( $R_x$ ,  $R_y$  and  $R_z$ ).
- An additional shear term appears when we integrate the shear production term of the TKE across the interface (neglected in KT).
- The horizontal momentum equations are now needed to compute the additional shear production term.

##### 1. The NPS mixed layer model equations

The three vertically integrated turbulent kinetic equations are :

$$\frac{\partial(h\overline{u'^2})}{\partial t} = 2M_3 \frac{(\tau_x/\rho)^2}{u^*} + (\Delta U)^2 w_e + R_x - \frac{D}{3} \quad (3.14)$$

$$\frac{\partial(\overline{h\nu'^2})}{\partial t} = 2M_3 \frac{(\tau_y/\rho)}{u^*} + (\Delta V)^2 w_e + R_y - \frac{D}{3} \quad (3.15)$$

$$\frac{\partial(\overline{hw'^2})}{\partial t} = -\alpha gh \frac{Q_o}{\rho C_p} + \beta gh S(e-p) - gh(\alpha \Delta T - \beta \Delta S) w_e + R_z - \frac{D}{3} \quad (3.16)$$

The right hand sides of Eq. 3.14 and 3.15 are the sum of several terms. The first term is the windstress part of the shear production where  $(\tau_x, \tau_y)$  are the components of the wind stress,  $\rho$  the density and  $u^*$  the friction velocity. It is followed by an additional shear production term associated with the jump in velocity  $(\Delta U, \Delta V)$  between the well-mixed layer and the entrainment zone.  $R_{[x,y,z]}$  and  $D$  are pressure redistribution and dissipation terms respectively. In Eq. 3.16, the entrainment buoyancy flux depends on the coefficients  $\alpha$  and  $\beta$  for thermal and salinity expansion, the temperature and salinity jumps  $\Delta T$  and  $\Delta S$  between the well-mixed layer and the entrainment zone.

The mixed layer temperature and salinity are given by Eq. 3.9 and Eq. 3.10.

The horizontal momentum equations are :

$$\frac{\partial(hU)}{\partial t} = f(hV) + \frac{\tau_x}{\rho} \quad (3.17)$$

$$\frac{\partial(hV)}{\partial t} = -f(hU) + \frac{\tau_y}{\rho} \quad (3.18)$$

$$\text{The mixed layer depth equation is given by : } \frac{\partial h}{\partial t} = w_e - \bar{w}_{-h} \quad (3.19)$$

where  $w_{-h}$  is the mean vertical velocity at the base of the mixed layer.

The system is now composed of 8 equations and 9 unknowns ( $T, S, h, R_x, R_y, R_z, D, U$  and  $V$ ). To compute the model, we will express some of the unknowns in term of total turbulent kinetic energy ( $E$ ) and use the TKE budget at the interface to get the ninth equation.



## 2. Special functions and constants

The friction velocity is defined by  $u^* = [(\frac{\tau_x}{\rho})^2 + (\frac{\tau_y}{\rho})^2]^{1/4}$  (3.20)

The net downward surface heat flux  $Q_o = Q_{\text{solar}} - Q_{\text{back radiation}} - Q_{\text{latent}} - Q_{\text{sensible}}$ .

The total TKE is :  $E = \overline{u'^2} + \overline{v'^2} + \overline{w'^2}$

In cases of usual mixed layer deepening, the dissipation  $\epsilon$  is parametrized by  $\frac{E}{\tau_D}$  where the dissipation scale  $\tau_D$  is a fraction (M1) of the time scale for one eddy rotation:  $\frac{h}{\sqrt{E}}$ . When mixed layers are very deep, the Rossby number is  $O(1)$  meaning that the planetary rotation has some influence on the water column motion. This can be taken into account by adding a fraction (M5) of the rotational time scale  $\tau_R = \frac{1}{f}$ . This yields a vertically integrated dissipation term:

$$D = \int_{-h}^0 \epsilon dz = 2M_1 \bar{E}^{3/2} + M5 f h \bar{E} \quad (3.21)$$

This says that dissipation will adjust to the supply of total kinetic energy  $E$  and is influenced by rotation.

The components of the pressure redistribution are modeled using a "return to entropy" theory:

$$R_x = 2M_2 (\frac{E}{3} - \overline{u'^2})E \quad R_y = 2M_2 (\frac{E}{3} - \overline{v'^2})E \quad R_z = 2M_2 (\frac{E}{3} - \overline{w'^2})E \quad (3.22)$$

The pressure redistribution can be viewed as an energy exchange between the three components of the TKE.

The key point in this model is the entrainment velocity  $w_e$ . An equation for  $w_e$  comes from the TKE budget at the interface. Since we are in a region where there is

negligible turbulence, the shear production and dissipation terms have sufficiently small contribution that they can be included in the remaining terms.

The unsteadiness term  $\frac{\partial \bar{E}}{\partial t}$  can be approximated by  $w_e \frac{\partial \bar{E}}{\partial z}|_{-h}$  or  $w_e \frac{\bar{E}}{h}$

The buoyancy flux term is now a big loss term and is rewritten using a fraction (M4) of the temperature and salinity jumps at the base of the mixed layer:

$$\frac{-\overline{\rho'w'}}{\rho_o}g = M4[\alpha g \overline{T'w'} - \beta g \overline{S'w'}] = M4[(-\alpha g \Delta \bar{T} + \beta g \Delta \bar{S})]w_e \quad (3.23)$$

Finally, the turbulent transport term is approximated by  $\frac{\bar{E}}{\tau_{w'}}$  with  $\tau_{w'} = \frac{h}{\sqrt{w'^2}}$  determined by the quantity of energy from  $E + \frac{p'}{\rho}$  carried by  $w'$ . Solving for  $w_e$ , we have:

$$w_e = \frac{\bar{E} \sqrt{w'^2}}{M4(\alpha g h \Delta \bar{T} - \beta g h \Delta \bar{S}) + \bar{E}} \quad (3.24)$$

Some asymptotic conditions, such as no stratification or free convection, can be applied to the model for basic verification. The results show that this entrainment model agrees with the extrem cases.

### 3. Role of each coefficients

The M coefficients introduced in these equations will be used later to tune the mixed layer model for application to deep convection. M1 and M5 quantify the dissipation, respectively for the TKE and rotation contribution. M2 is the pressure redistribution coefficient, which only appears in the individual vertically integrated TKE equations. It quantifies the energy exchange within the TKE budget. M3 quantifies the role of the shear production and therefore the windstress. M4 weights the buoyancy flux and indirectly the entrainment velocity term.

## E. THE NPS SIMULATION

In that series of simulations, we will first set the references by looking at both constant and variable atmospheric forcing under normal conditions (specified later). Then we will briefly estimate the influence of the Coriolis parameter, and finally assess the role of each 'M' coefficient to try to predict the observed states.

The initialization is done with the same initial conditions as the KT simulation (initial temperature and salinity profiles of Fig. 5) and the program runs for the same ten-day period.

### 1. Simulation under normal conditions

The normal conditions refer here to a Coriolis parameter taken at the mean latitude of the convection area and the M coefficients determined for a usual mixed layer deepening (non convection type). These coefficients are set to  $M1=1$ ,  $M2=0.5$ ,  $M3=6$ ,  $M4=1$  and  $M5=1$  (Garwood 1977).

#### *a. Constant atmospheric forcing*

The constant values used as input for the atmospheric forcing are the ten-day heat flux and friction velocity means. Besides deepening to 450 meters (Fig. 15), the smoothed curves are similar to the simulation using the KT model. The rate of deepening is fairly constant over the period; the peak temperature is reached after one day, and the final values for temperature, salinity and density are again close to the observed ones but slightly lower than with the KT simulation.

#### *b. Variable atmospheric forcing*

The shape of all curves (Fig. 16) reflects the variations in the atmospheric forcing, being flat when the forcing is small and steeper when the forcing increases. This results in delaying the temperature peak because of the delay in the surface forcing. The final mixed layer depth is 500 meters and all the other final values are the same as for the constant forcing simulation.

As in the previous section, the comparison of the simulated temperature at 530 meters and the in-situ recording (Fig. 8) will not be conclusive. Since the mixing

reaches only 500 meters, the plot would simply show a flat curve at 12.8°C for the simulated temperature at 530 meters!

## **2. Role of the Coriolis parameter**

Using a variable atmospheric forcing and the same values for the M coefficients, let's try to see the influence of rotation. The most visible effect of rotation is to decrease the final mixed layer depth as the Coriolis parameter increases (Fig. 17). for  $f=0$ , the final depth is 1400 meters or more than twice the value of  $f > 0$ . With and without rotation, the deepening rate is the same up to 250 meters or five days after the beginning of the convection, but it dramatically increases after when there is no rotation. The temperature and salinity jumps are above 250 meters. Therefore once the mixed layer depth reaches 300 meters, all the mixing is completed. For that reason, the final temperature, salinity and density values remain the same as for the previous cases.

An explanation of this interesting result can be found in Garwood (1977) who describes the general solution of the NPS model in terms of dimensionless parameters. He stated that the nondimensional mixed layer depth  $Z^*$  is directly proportional to the inverse boundary-layer Rossby number and thus proportional to the Coriolis parameter. The boundary-layer Rossby number ( $Ro$ ) is the ratio of the friction velocity  $u^*$  to the Coriolis parameter. The rate of entrainment decreases with an increasing  $Z^*$  or an increase in layer stability. Then it takes more time for the mixed layer to deepen at mid-latitudes than at the equator. For the same time period the mixed layer depth will be larger at the equator than at mid-latitudes. We can also state that in deep convection, the overturning creates large eddies which can be influenced by rotation. Thus, when there is no rotation, the deepening is more important.

## **3. The influence of the M coefficients**

### ***a. Search for the best coefficients***

All five coefficients influence the rate of mixed layer deepening. The goal is to determine the correct magnitude or weight of each coefficient in order to successfully simulate a deep convection event. A simple doubling or halving of each coefficient one at

a time already shows significant changes in the mixed layer depth and temperature. Figure 18 shows the variation of these two quantities with respect to the variations of each coefficient. The solid curve serves as a reference; it is taken from the previous run which was done for a variable forcing, a Coriolis parameter taken at the Mediterranean latitude and the M coefficients at  $M1=1$ ,  $M2=0.5$ ,  $M3=6$ ,  $M4=1$   $M5=1$ .

All coefficients seem to have a important effect on the deepening rate. The mixed layer depth increases significantly for a decrease in  $M1$ ,  $M4$  and  $M5$  and an increase in  $M2$  and  $M3$ . All the temperature curves have the same shape and final value.

Is there a reasonable explanation for the way the coefficients must be changed? The dissipation is linked to the TKE by  $M1$  and to the Coriolis parameter by  $M5$ . Since the convection occurs to deep levels, the TKE in the water column is very large and the rotation may have a large influence on the column. Decreasing  $M1$  and  $M5$  is needed to compensate for the large quantity of TKE produced and to reduce the influence of rotation. From the Kraus and Turner simulation, it was found that the buoyant production was a more efficient source of mixing than the shear production. Therefore, we can conclude that (1) since at great depth the wind is no longer felt,  $M3$  must increase to keep a relative influence of the wind; (2) consequently  $M3$  has to increase to balance the terms of the TKE equations; and (3)  $M4$  has to decrease to reduce the influence of the efficient buoyancy flux. Decreasing  $M4$  increases the entrainment velocity which is the case during the convection events.

#### ***b. A NPS simulation with deep convection coefficients***

An investigation of the best coefficients is now possible by each time doubling  $M2$  and  $M3$  and halving  $M1$ ,  $M4$  and  $M5$ . Other choices for the coefficients are possible, but this one respects the initial ratio between  $M1$ ,  $M2$ ,  $M3$ ,  $M4$  and  $M5$  and favors the rapidity of the process.

Plotted on Fig 19, the increase in the coefficients shows a MLD reached sooner, thus an earlier mixing with the warmer and saltier intermediate water. We also notice that in the case of deep convection coefficients, the mixed layer depth responds to the

significant forcing occurring after the second day whereas the temperature, salinity and density are mixed within the first few hours. This is consistent with the definition of violent mixing in the second chapter. The coefficients kept for the NPS deep convection case are  $M1=0.125$ ,  $M2=4$ ,  $M3=48$ ,  $M4=0.125$  and  $M5=0.125$ .

*c. Validity of the coefficients found*

There are a few ways to assess the validity of the coefficients. First by looking at the time series of the TKE provided by the model for the 2500 meters water column and comparing it with the mean in-situ TKE at 450 meters. As the coefficients evolve, Fig. 20 shows an increase in the mean value of modeled TKE as well as a better fit for the in-situ TKE. The increase in TKE must be compensated by a decrease of  $M1$ .

Then going back to the way Garwood (1977) found the values for its coefficients, we can try to apply the same method in our deep convection case. The easiest coefficient to compute is  $M3$ .  $M3 = \frac{\partial U(0)}{u^*}$  where  $u^*$  is the friction velocity and  $\delta U(0)$  the magnitude of the mean velocity associated with the mean shear. The computation using in-situ data for  $U$  and  $V$  gives  $M3 \approx 10$ .

The simulated temperature at 530 meters with deep convection coefficients (Fig. 10) shows a better agreement with the observed result.

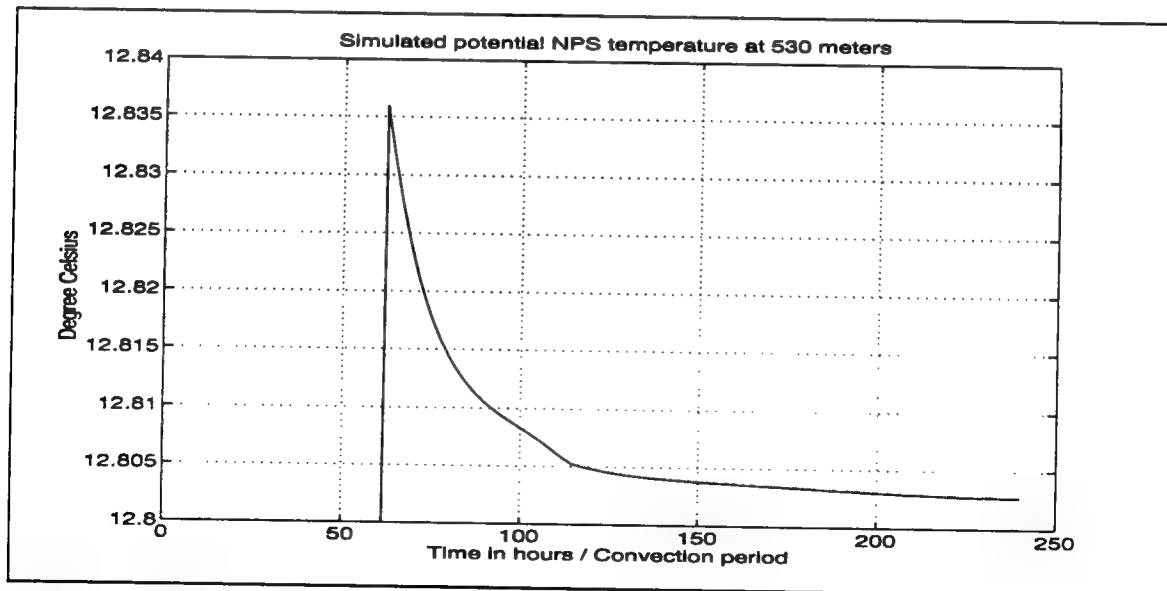


Figure 10. Reconstituted Temperature at 530 Meters with Deep Convection Coefficients.

After the interface has reached the level 530 meters, the reconstituted temperature shows a decrease, similar in magnitude to the observed one, but much quicker in time. This only proves that there was some improvement compared to the Kraus and Turner method, but we still need a better fit of the coefficients.

Using in-situ data and a computation of the TKE budget from Eq. 3.10, we can estimate the mean dissipation in the case of deep convection, providing values for M1 and M5 using Eq. 3.21. This yields M1 and M5  $O(0.1)$  which is consistent with the previous estimation.

## F. SUMMARY OF THE SIMULATIONS

	Forcing type	Coriolis Parameter	Kraus & Turner model	Naval Postgraduate School model
Usual coefficients	Constant forcing	$f=0$	MLD 950 meters	MLD 1250 meters
		$f=42$		MLD 450 meters
	Variable forcing	$f=0$	MLD 1150 meters	MLD 1400 meters
		$f=42$		MLD 500 meters
Optimized coefficients	Variable forcing	$f=42$	MLD 2500 meters after 215 hours	MLD 2500 meters after 75 hours

Table 1. Summary of the Mixed Layer Depth Reached using the Kraus and Turner Model and the Naval Postgraduate School Model.

## **G. PARTIAL CONCLUSION AND RECOMMENDATIONS**

The two simple and one-dimension models were used to evaluate the long term evolution of the mixed layer characteristics. The final computed values are almost the same as the observed values. However, with the tuning coefficients set for a normal mixed layer deepening, the correct final state is only achieved after ten days. The 1987 Mediterranean deep convection event was achieved over only a few hours. That was be the major difference found between the models and the in-situ data. With some adjustments in the tuning coefficients, the models can approach the rapidity of the actual event. But those models do not have the physics of the deep convection built in so the change of the parameter's value may be irrelevant.

We can recognize the ability for these simple models to produce believable long term results and need to look at 3-dimensional models. Among them, a non-hydrostatic large eddy simulation (LES) model (Moeng 1984) was adapted to ocean mixing. In the atmosphere as well as in the ocean, the LES model attempts to simulate the large scale structure of the convection process (simulation of large eddies produced by the instabilities of the mean flow) and parameterize the smaller eddies that derive from bigger eddies by an energy-cascade process. Thus, solving the primitive equations (momentum, continuity, temperature and salinity) for the dynamic variables separated into large eddy fields (mean quantities) and subgrid-scale fluctuations (turbulent quantities), the LES model provides the evolution of the velocity, temperature, and salinity fields as well as the statistic of the turbulent quantities. The first runs of this model under a constant forcing seem promising.



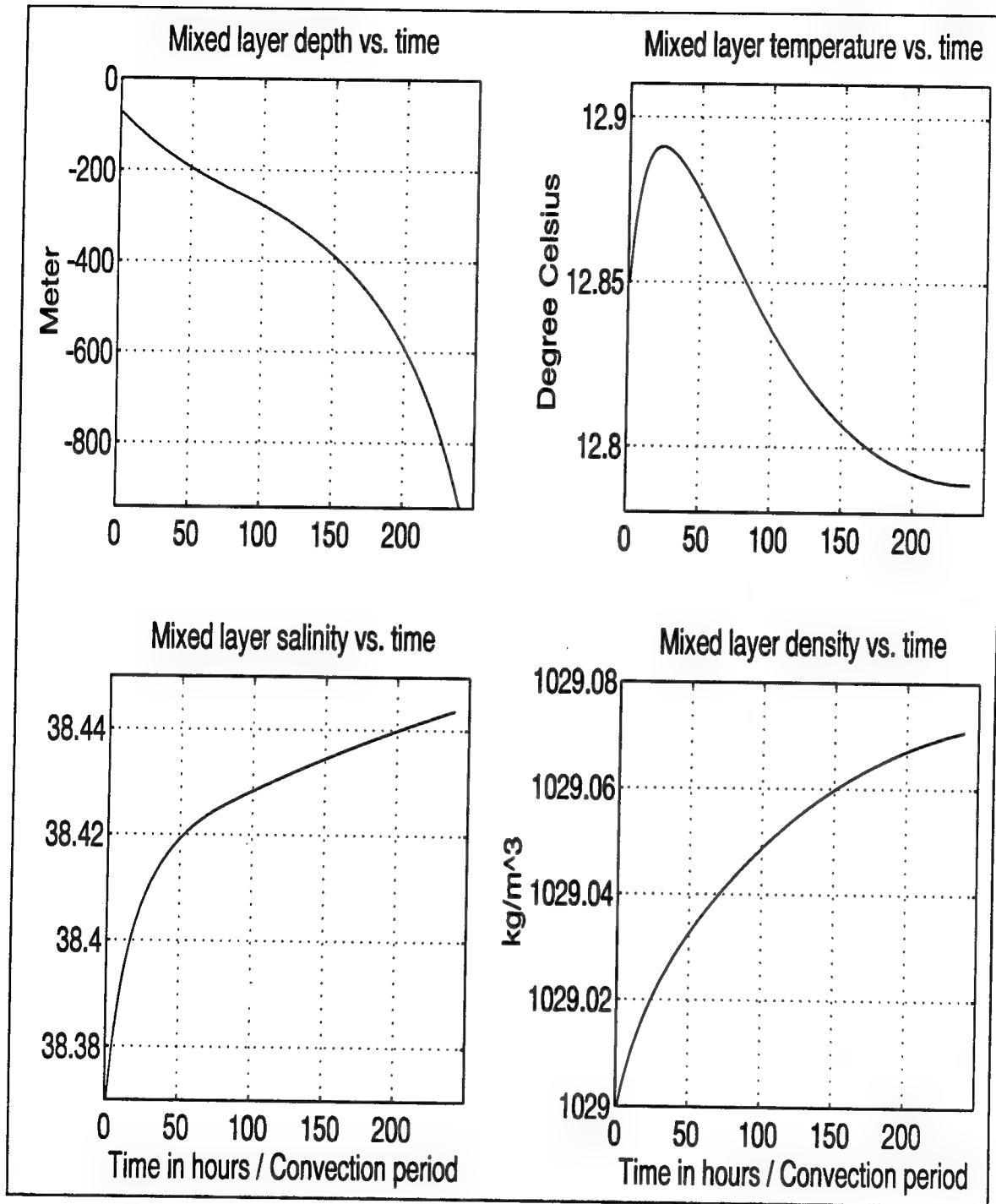


Figure 11. Kraus and Turner Simulation of the Variation of Mixed Layer Depth, Temperature, Salinity and Density with Time under Constant Windstress and Heat Flux.

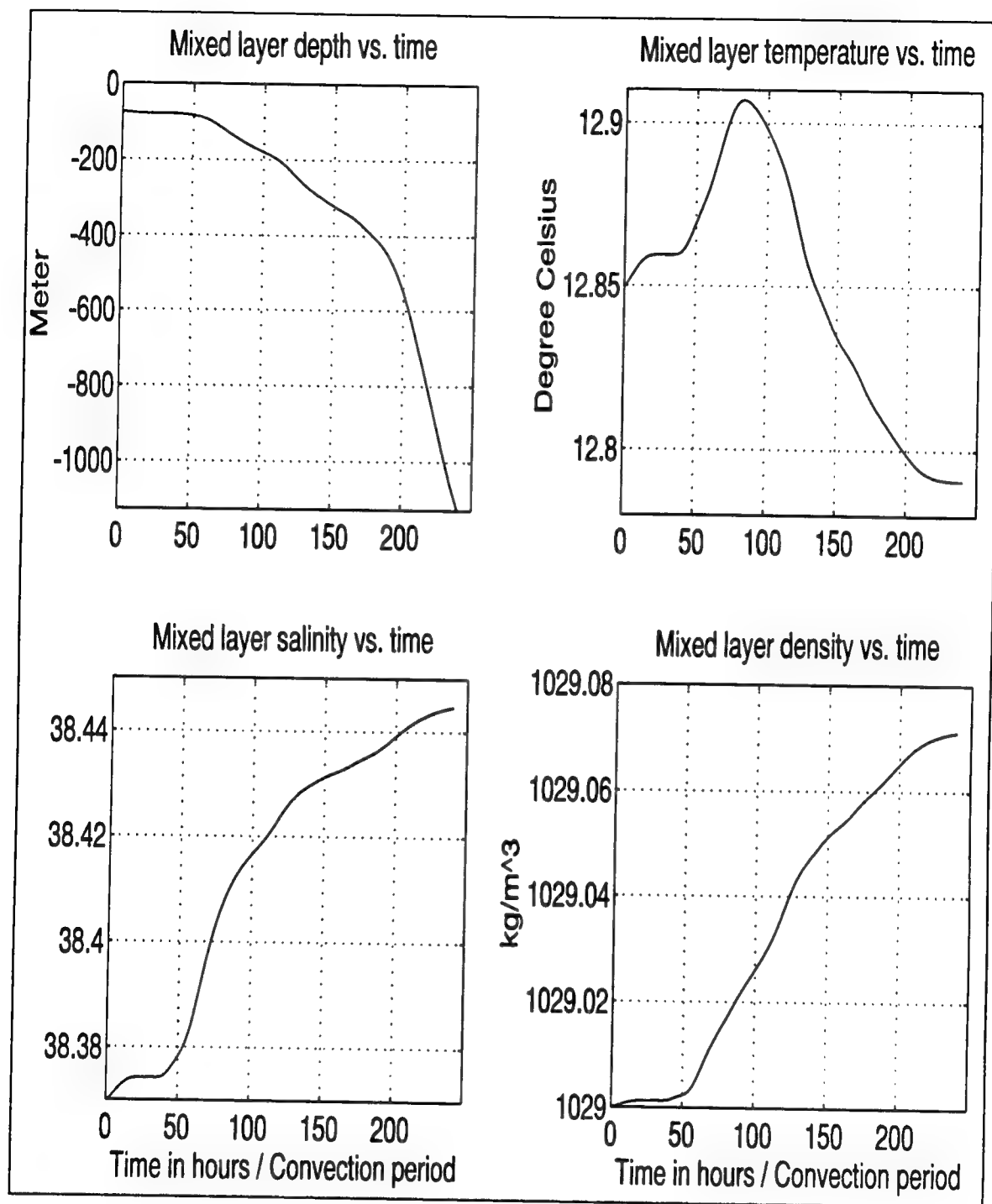


Figure 12. Kraus and Turner Simulation of the Variation of Mixed Layer Depth, Temperature, Salinity and Density with Time under Actual Windstress and Heat Flux.

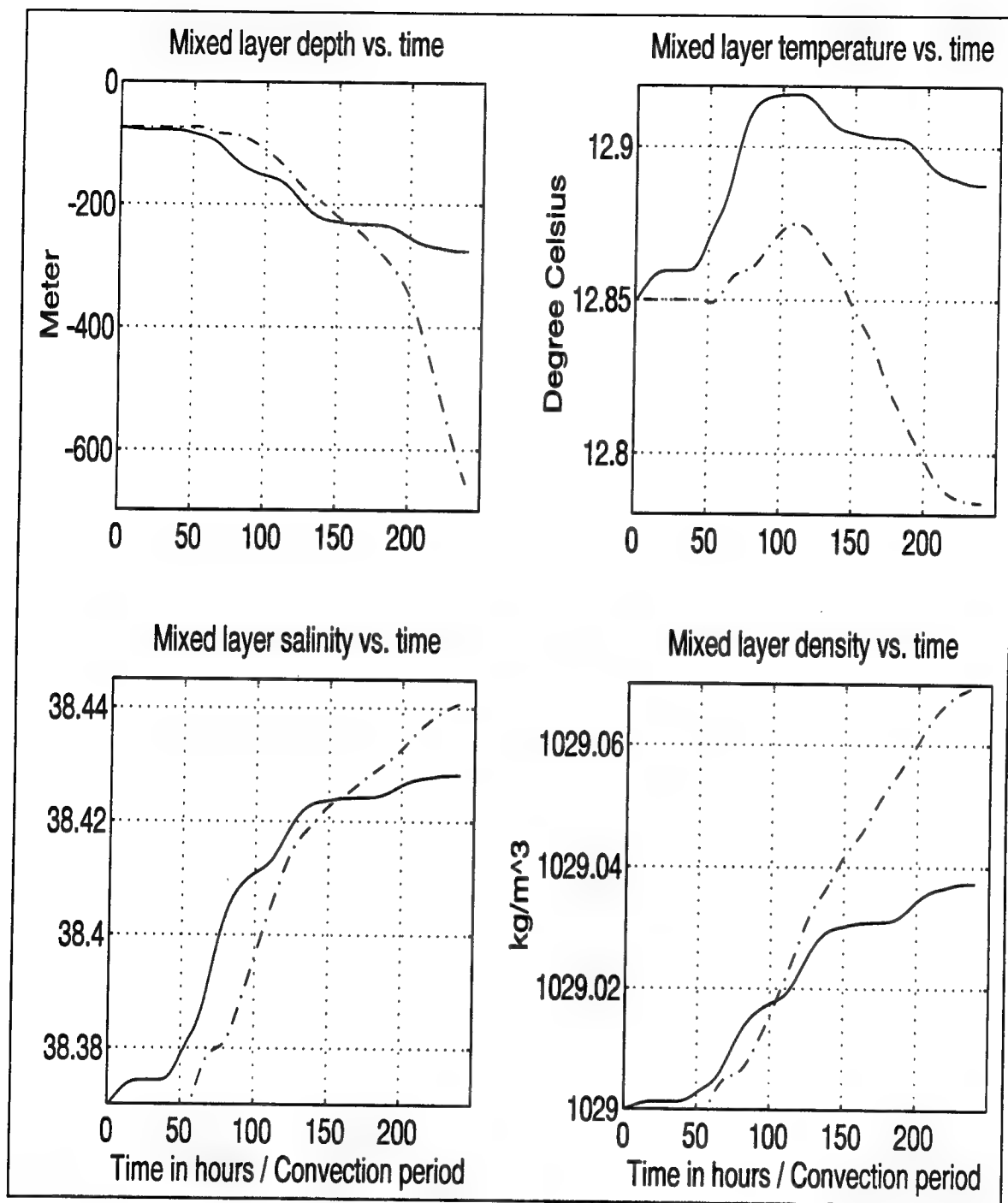


Figure 13. Kraus and Turner Simulation of the Variations of Mixed Layer Depth, Temperature, Salinity and Density with Time under Actual Windstress (--) or Heat Flux (-.-).

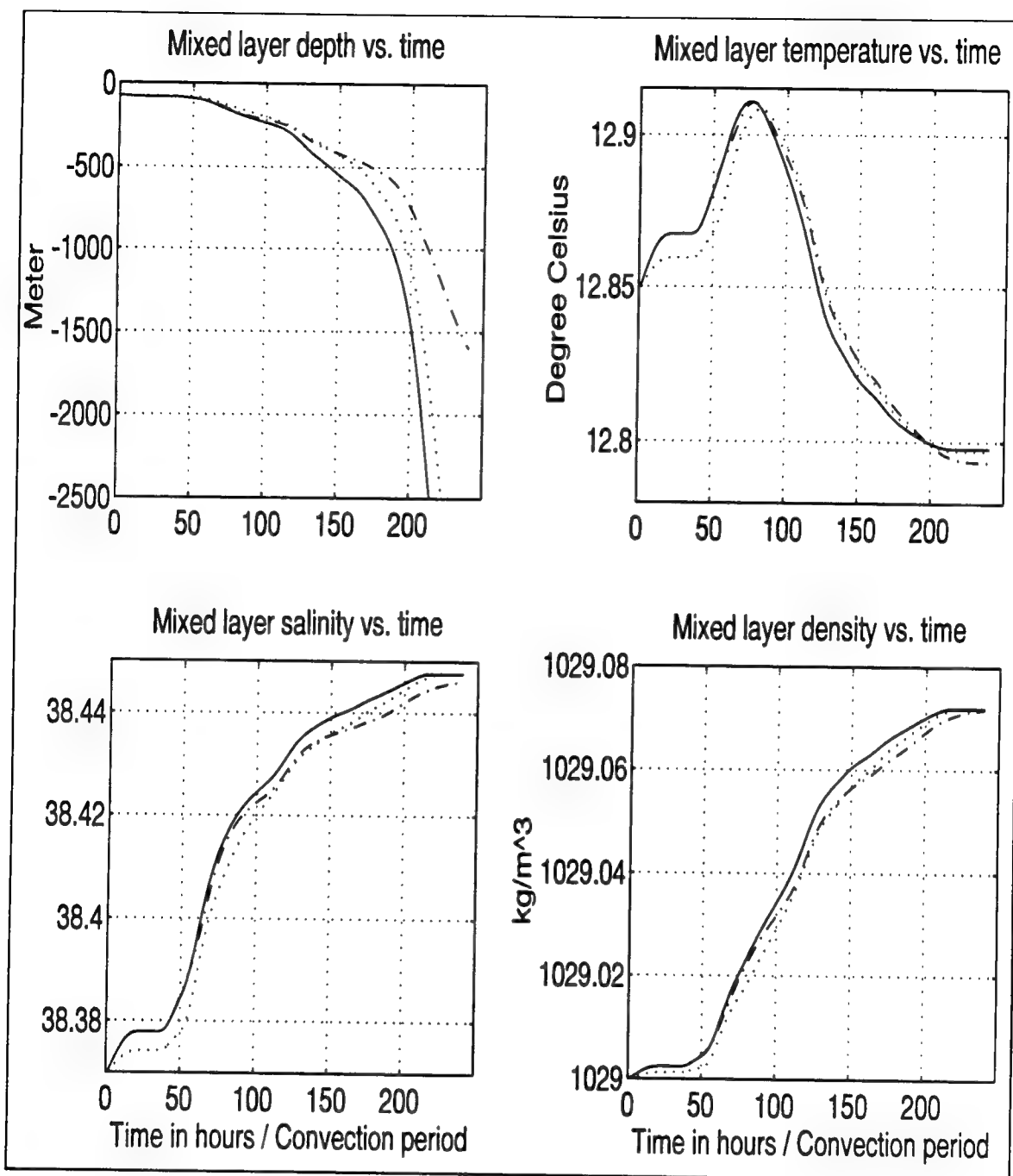


Figure 14. Kraus and Turner Simulation of the Variation of Mixed Layer Depth, Temperature, Salinity and Density with Time under Actual Windstress and Heat Flux using Adjusted Coefficients ( $c1=1, c2=2$  (.....) /  $c1=2, c2=1$  (-.-.-) /  $c1=2, c2=2$  (----) ).

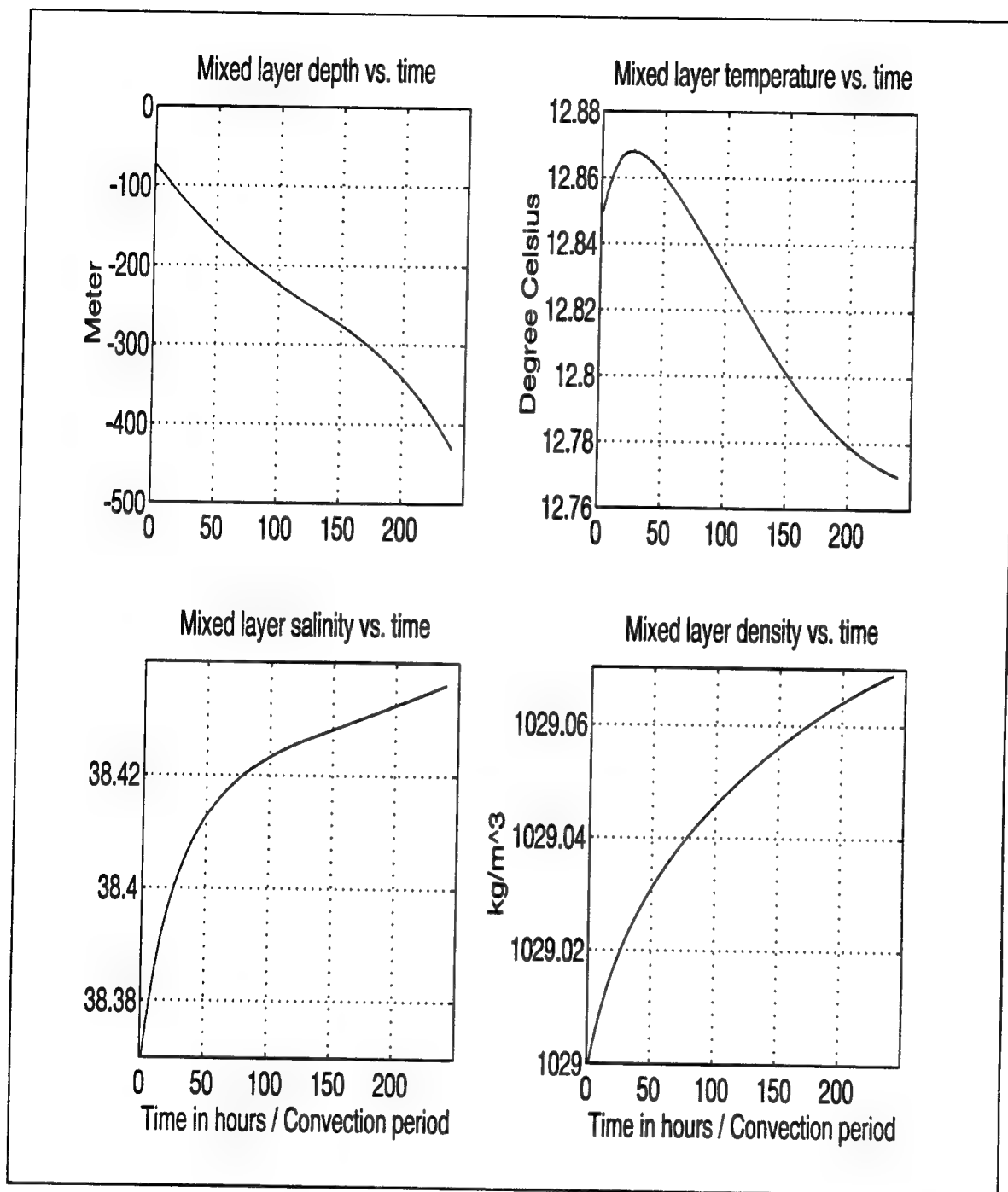


Figure 15. Naval Postgraduate School Simulation of the Variation of Mixed Layer Depth, Temperature, Salinity and Density with Time under a Constant Windstress and Heat Flux.

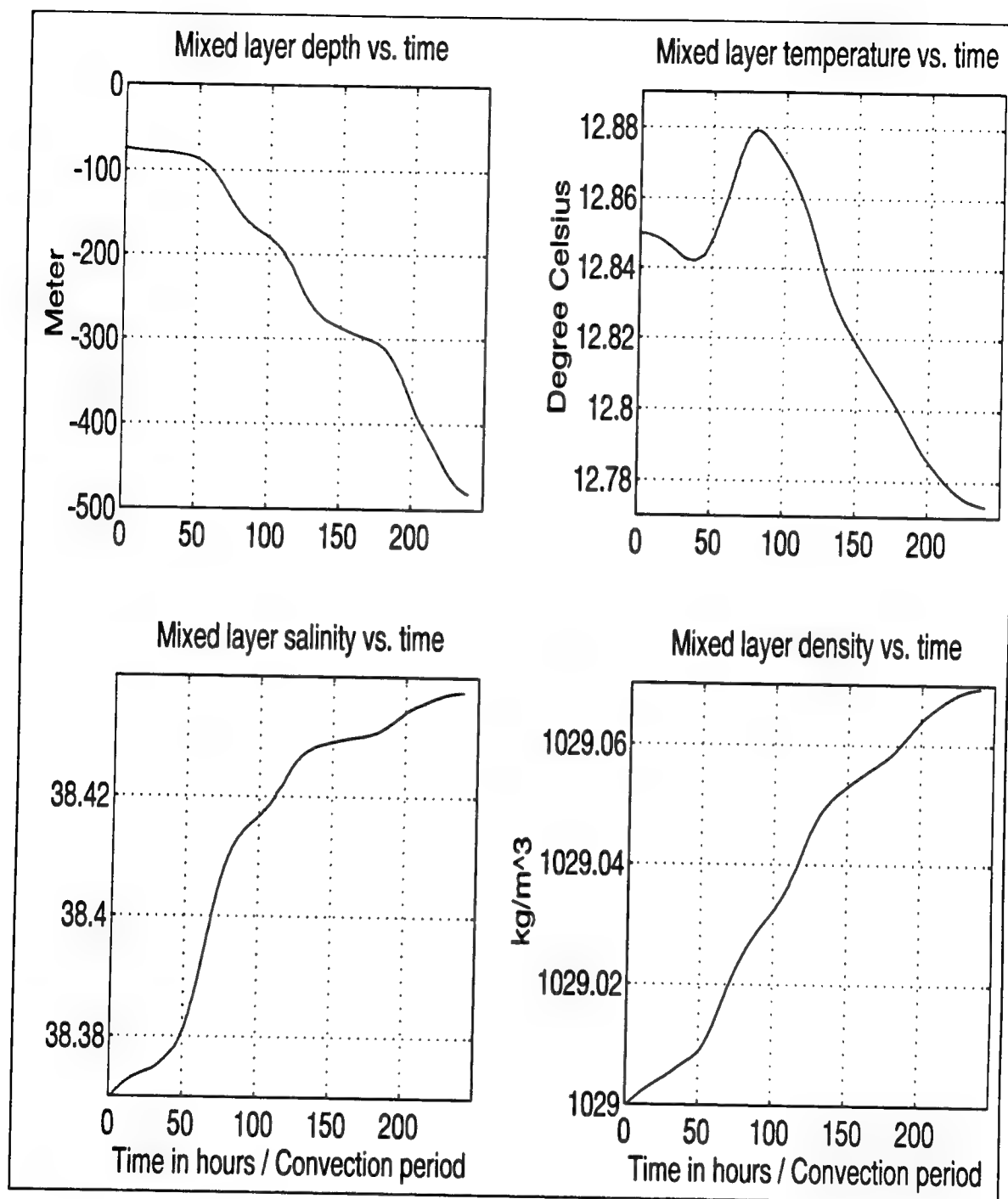


Figure 16. Naval Postgraduate School Simulation of the Variation of Mixed Layer Depth, Temperature, Salinity and Density with Time under Actual Windstress and Heat Flux.

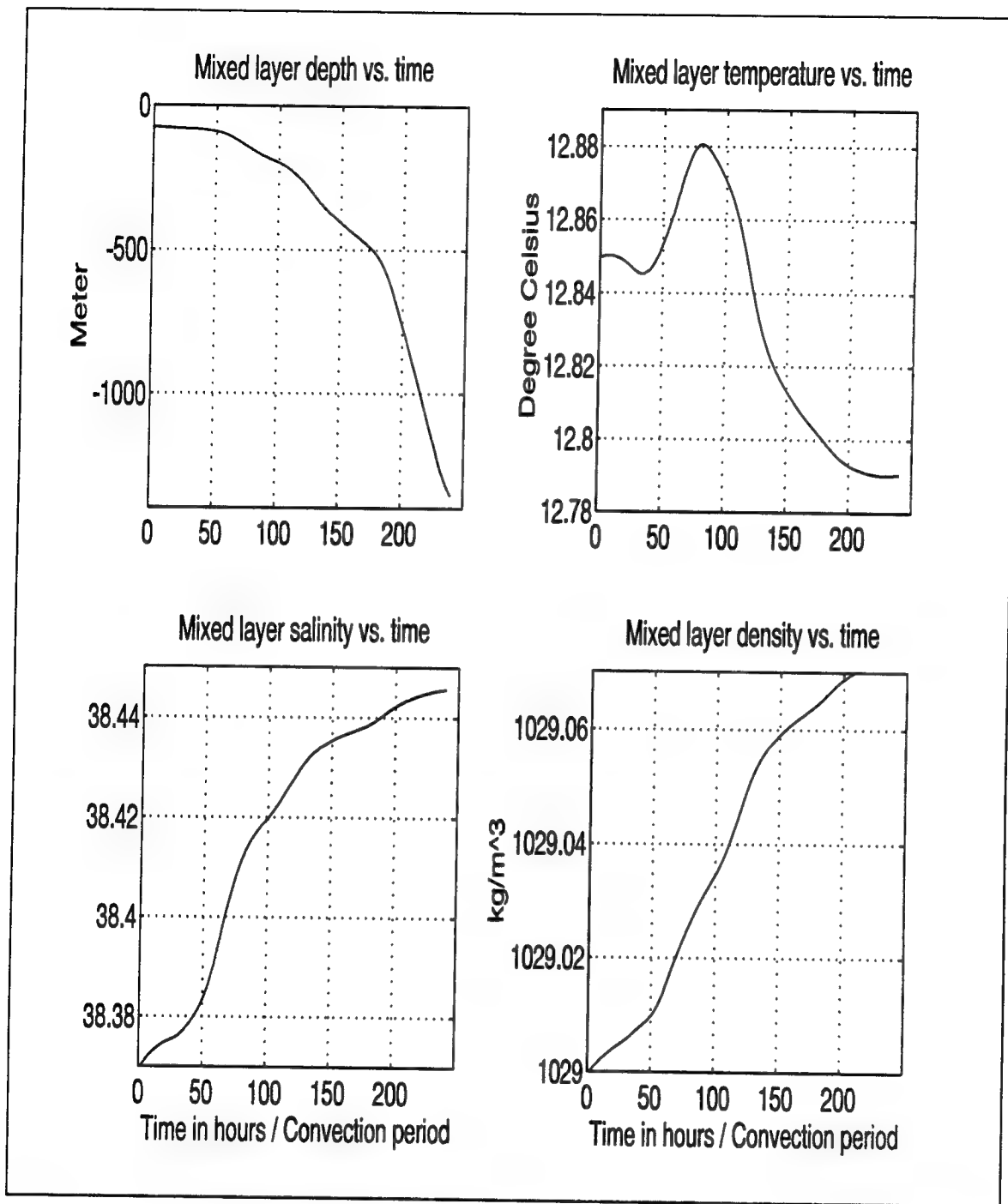


Figure 17. Naval Postgraduate School Simulation of the Variation of Mixed Layer Depth, Temperature, Salinity and Density with Time under Actual Forcing and No Rotation.

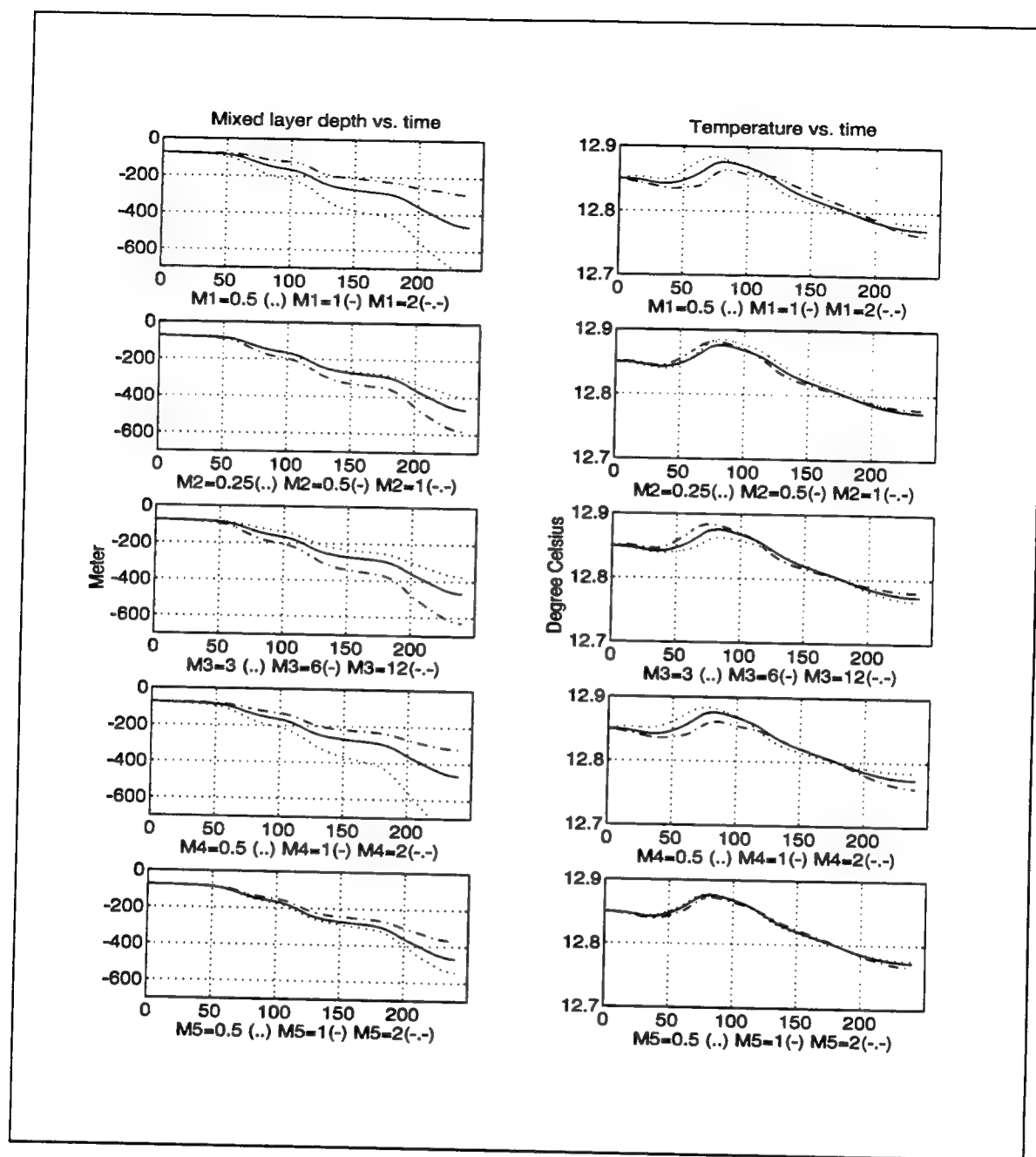


Figure 18. Search for the Best Set of Coefficients. Naval Postgraduate School Simulation of the Variation of Mixed Layer Depth and Temperature with Time under Actual Wind-stress and Heat Flux using Different Sets of Coefficients.



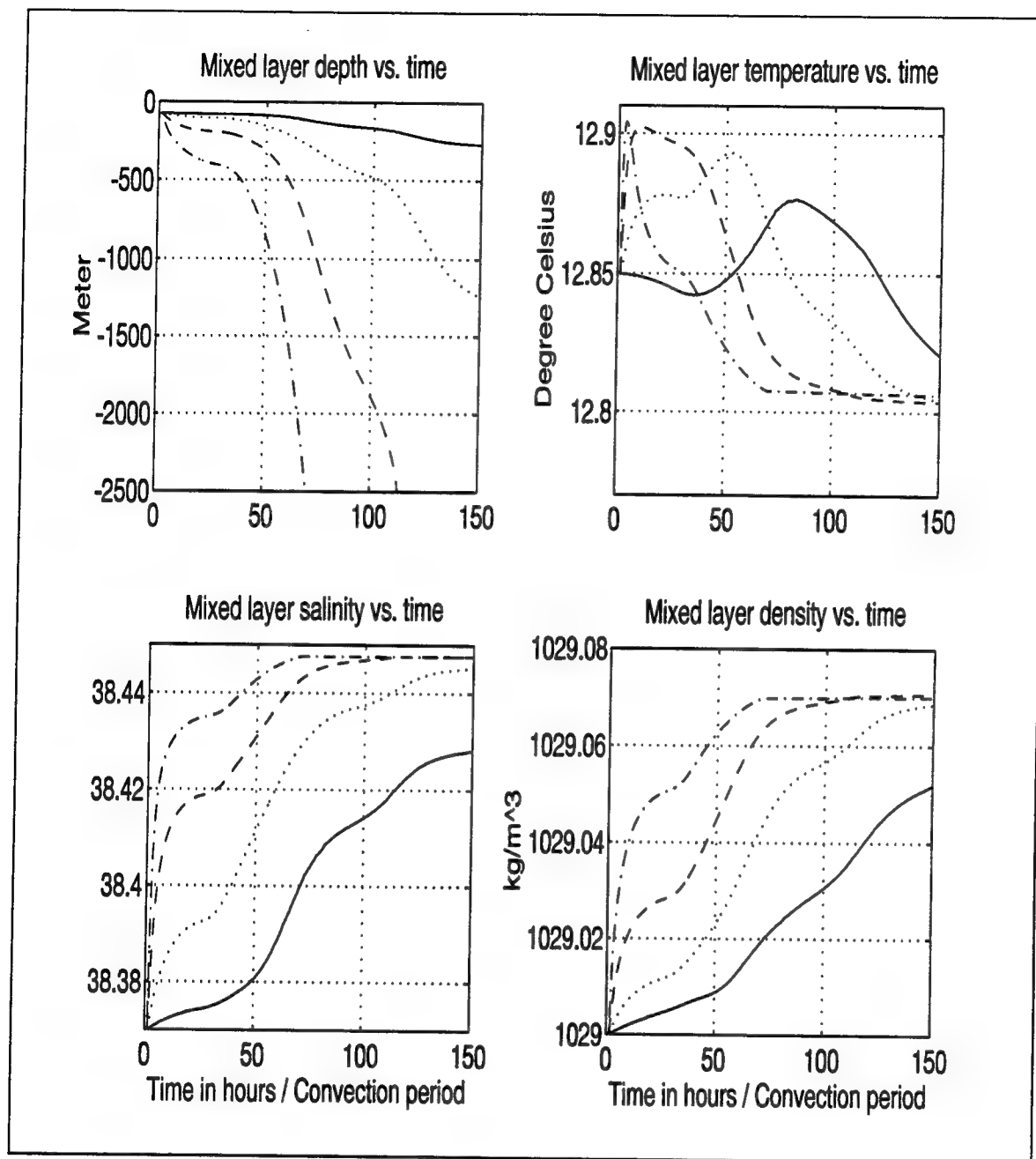


Figure 19. Naval Postgraduate School Simulation of the Variation of Mixed Layer Depth, Temperature, Salinity and Density with Time under Actual Forcing using Different Coefficients: ((M1, M2, M3, M4, M5) = (1, 0.5, 6, 1, 1)(---) / (0.5, 1, 12, 0.5, 0.5)(.....) / (0.25, 2, 24, 0.25, 0.25) (- - -) / (0.125, 4, 48, 0.125, 0.125) (-.-.-)).

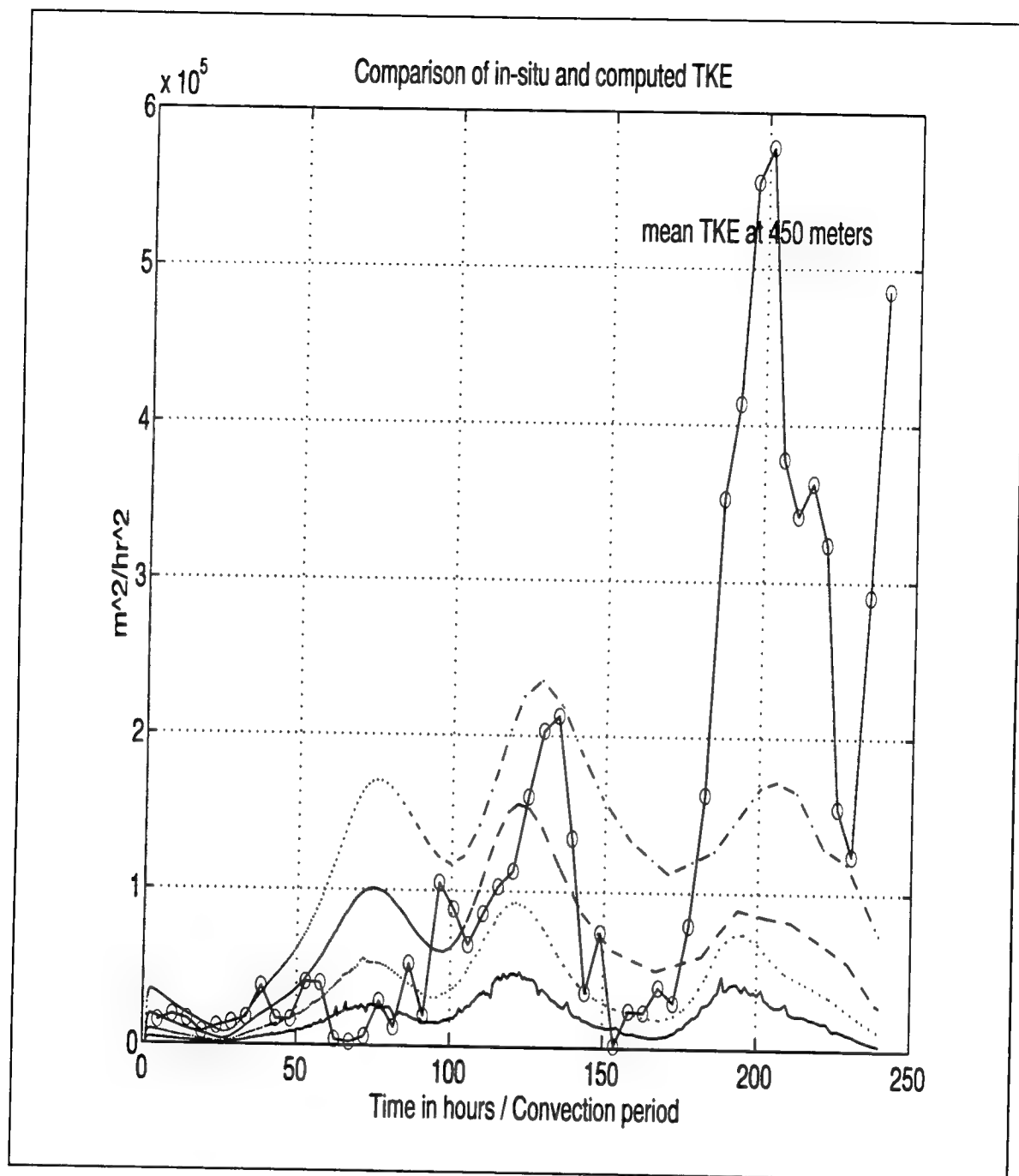


Figure 20. Time Series of Mean In-situ Turbulent Kinetic Energy at 450 meters and Turbulent Kinetic Energy Produced by the Naval Postgraduate School Model under Actual Forcing using Different Coefficients (labelled as in Fig. 19).

## **IV. REMOTE SENSING AND DEEP CONVECTION**

### **A. MOTIVATION**

#### **1. Previous work on the subject**

During the past decade, satellites have proven to be very useful in measuring and understanding characteristic features of the ocean. Currents, sea surface temperature, surface winds, sea surface level, waves and biological activity are some examples where our knowledge has considerably improved through the use of satellite data. Altimeter, Synthetic Aperture Radar (SAR) and Advanced Very High Resolution Radiometer (AVHRR) are the most significant instruments.

Detection of deep convection from orbiting platforms has rarely been attempted. European Remote Sensing Satellite ERS-1 SAR images of the Greenland sea have been compared (Carsey and Garwood 1993) to the Large Eddy Simulation (LES) model of Moeng (1984) adapted to ocean convection (Garwood et al. 1994) for the winter of 1992. The ice covered convection area (20 x 90 km) shows a "ragged net" pattern that was simulated by the model. The convection zone contains small, warm cells (~ 1 kilometer in diameter) of upwelling water surrounded by sinking, cold water. The cells rotate anticyclonically and, in fact, are visible through the imprint they leave on the first-year ice. These encouraging results open the door to further investigation of deep convection processes using satellites.

To date, deep convection in the Golfe du Lion has not been examined using remote sensing. However, GEOSAT altimeter data are available for that area and studies of general Mediterranean sea surface heights have been conducted (Arabelos and Tziavos 1990).

Sea surface height studies have been conducted in all parts of the world ocean. Their results cover mainly currents (Gulf Stream), circulation (Southern ocean), bathymetric features (Gulf of Mexico) and oceanic events (El Nino). For more information, the reader should refer to the two Journal of Geophysical Research special issues (March and October 1990) devoted to GEOSAT altimeter results.

A attempt was made to look at AVHRR images of the Golfe du Lion during the convection period. Due to the cloud coverage only two images were available. The precision of the radiometer as well as the software used to exploit the images were not sufficient to detect the temperature evolution of 1/10 degree related to the convection process.

The investigation of deep convection using remote sensing instruments will be done with the GEOSAT altimeter data.

## 2. Theoretical computation of the observable signal

A preliminary and simple computation of the theoretical sea surface height during a convective event can be done using first a geostrophic computation and a mass conservation type computation. The geostrophic (4.1) and hydrostatic (4.2) equations can be combined (4.3) to approximate the slope of the sea ( $\eta$ ) surface level as a function of the surface velocity ( $u,v$ ).

$$fv = \frac{1}{\rho} \frac{\partial P}{\partial x} \quad fu = -\frac{1}{\rho} \frac{\partial P}{\partial y} \quad (4.1)$$

$$\partial P = \rho g \partial \eta \quad (4.2)$$

$$fv = g \frac{\partial \eta}{\partial x} \cong g \frac{\Delta \eta}{\Delta x} \quad \text{or} \quad \Delta \eta = \frac{fv \Delta x}{g} \quad (4.3)$$

With a surface circulation of 0.1 to 0.2 m/s and an elliptical shape area of deep convection whose major axis is 100 kilometers, the expected sea surface height variation should be 10 to 20 centimeters.

The sea surface variation inferred from the mass computation is given by:

$$\sum \{ [h(i+1) - h(i)] * [\rho(i+1) + \rho(i)] / 2 \} = \rho_{cv} h_{cv} \quad (4.4)$$

where  $h(i)$  [ $\rho(i)$ ] is the depth [density] of the  $i^{\text{th}}$  layer,  $h_{cv}$  [ $\rho_{cv}$ ] the depth [density] reached after the convection (here bottom = 2000 meters). Using the density profiles before and

after the convection process (Leaman and Schott 1991) the sea surface variation should be O(15 centimeters). These two simple computation show that the expected signal is at least greater than the altimeter accuracy, and therefore should be observable.

## **B. THE GEOSAT ALTIMETER**

### **1. The geodesy satellite**

The GEOSAT (Geodesy satellite) was launched on March 12, 1985, into a 108-degree inclination, 800-kilometer altitude orbit. The primary mission provided 18 months of altimeter data required to improve the accuracy for the measurement of the earth's gravitational field. In October 1986, GEOSAT was maneuvered into a 17-day exact repeat orbit in order to detect mesoscale oceanographic features. The system then provided a ground-track separation of 164 kilometers at the equator and 110 kilometers at midlatitudes (John Hopkins APL 1987). The GEOSAT program ended in October 1989 due to a failure in the recording system.

### **2. The principle of the altimeter measurement**

The principle of satellite altimetry is very simple. Short radar pulses are reflected from the Earth. The satellite height is deduced from the two-way travel time of the pulse. The altimeter measures the height of the satellite above the sea surface ( $H_s$ ).

The topography ( $H_t$ ) is the departure of the ocean surface from the geoid and is influenced by oceanic features. The orbit height ( $H_o$ ) and the geoid height ( $H_g$ ) are the heights of the satellite orbit and the geoid above an arbitrary reference surface, generally chosen to be an ellipsoid. To measure the ocean topography, we must combine the heights,

$$H_t = H_o - H_s - H_g \quad (4.4)$$

The geoid and the time independent errors are a permanent signal ( $H_g$ ) that can be computed by taking the mean of the satellite height ( $H_t+H_s$ ) over a certain period. The orbit height ( $H_o$ ) is obtained by a worldwide ground-based tracking network.

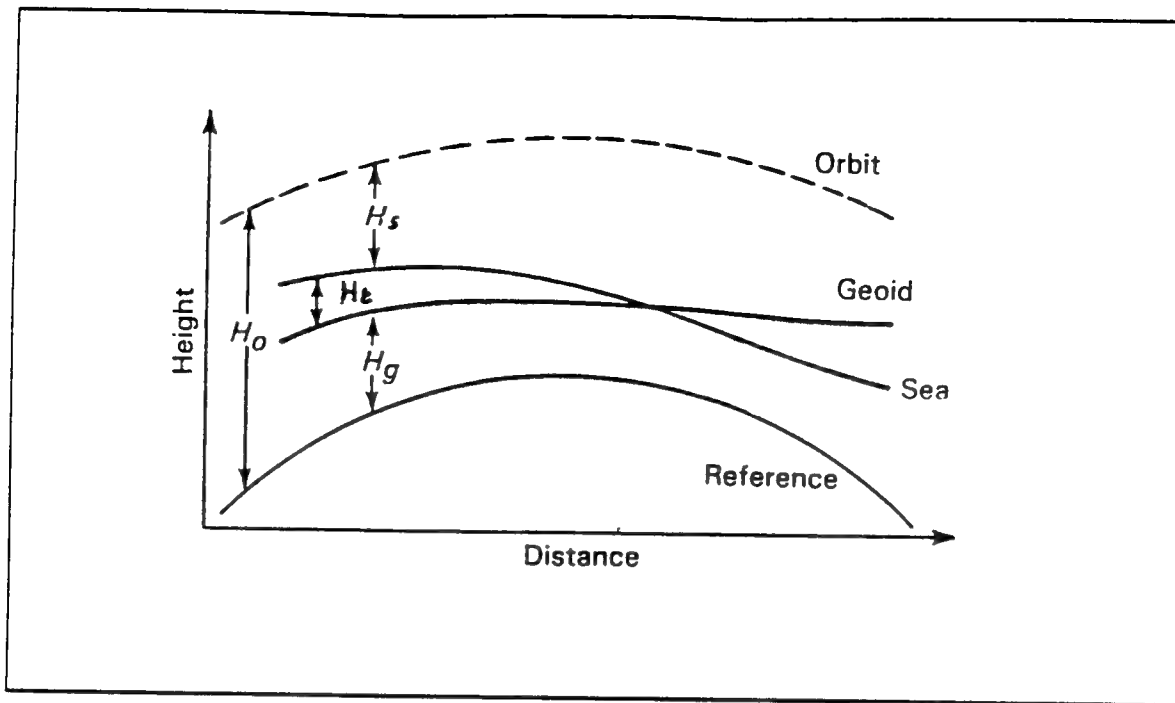


Figure 21. The Altimeter Measurement System. From John Hopkins APL, 1987

### 3. The altimeter characteristics

The GEOSAT altimeter is a 13.5-gigahertz nadir looking pulse compression radar. Estimation of three parameters is possible from processing the pulse compression data: height (distance between the satellite and the sea) with a precision of 3.5 centimeters for a 2 meters significant wave height (SWH); SWH, with generally a precision of 0.5 meters and wind speed with 1.8 meter per second accuracy over the range 1 to 18 meters per second.

### 4. Typical altimeter problems

Instrumental and environmental corrections due to atmospheric water vapor, dry gases, ionosphere and ocean waves and tides need to be known to have accurate height measurements. Moreover, since the orbit is the reference frame (Stewart 1985) for the measurements, a special attention must be paid to the orbit error correction in altimeter computations.

The orbit error is the sum of the radial error (error on satellite height), the along-track error (satellite ahead or behind its theoretical position on the orbit; this can also be treated as a height error) and the ground-track error (satellite left or right of its theoretical orbit). The clock error (sampling at an inappropriate time) can also occur but will be treated as an along-track error (Stewart 1985). Consequently the satellite orbit error reduces to a ground-track and a height error.

The ground track error can be solved using a crossover adjustment or an interpolation whereas the orbital error can be minimized by either crossover adjustment or a collinear technique. In all the cases, these types of error are difficult to model and to correct. The overall altimeter precision is the sum of all its errors and can be estimated to ten centimeters.

## **C. DATA ANALYSIS**

### **1. The altimeter data**

The data were extracted from CDs-ROM available at the Oceanography Department of the Naval Postgraduate School. The CDs cover the entire Exact Repeat Mission (ERM): November 1986 through October 1989. Using the GEOSAT daily file, equator crossing list, orbit corrections file and mean tracks files as input, a FORTRAN program returns the height, time, latitude and longitude of the observations along each elementary track crossing the chosen domain. An option in the program enables the observed heights to be corrected for the wet and dry tropospheric error, the ionospheric error, the solid and ocean tides and the inverse barometer effect. Orbit correction does not exist and special attention must be given to this problem.

### **2. The corrections applied to the data**

The orbit correction was estimated in two steps. First, a two year mean (November 1986 - October 1988) of the global orbit was removed. Then the residual bias on each individual track was removed by subtracting the residual mean at that particular time and location. The importance of bias removal can be seen on Fig. 24 and 25. After this orbit

correction, the remaining signal mainly lies between -10 and 10 centimeters with a few exceptions consistent with the theoretical computation.

In areas where the geoid gradient is large (such as the conelike topography of the Golfe du Lion), we must look carefully at the cross-track error. An easy way to check the size of this error is to compute the geoid with the 2 year mean tracks used for orbit correction. This was done using the multiquadric interpolation program described later and produce a Western Mediterranean geoid close to the observed one. Therefore, we can conclude that the cross-track errors are small during this computation.

Two atmospheric corrections were applied. The wet tropospheric correction was deduced from the measurements by the NOAA TIROS (Television and Infrared Observation Satellite) operational vertical sounder (TOVS) or the Special Sensor Microwave Imager (SSM/I) on board the Defense Meteorological Satellite (DMSP). This wet tropospheric correction is induced by the water vapor present along the altimeter path. The propagation velocity of a radio pulse is also slowed by the dry gases present in the Earth's atmosphere. The chosen dry tropospheric correction is determined from a model assimilating data from the European Center for Medium Range Weather Forecasting (ECMWF).

The inverse barometer effect, which is the hydrostatic response of the sea surface to the atmospheric pressure was assumed to be a constant over the small area considered.

No tidal correction was made because no good tidal model was available for the Mediterranean. However, the error can be estimated. The M2 tide seems to be dominant in western Mediterranean sea and has an amplitude of 5-6 centimeters and a constant phase of 230° across the basin (Sanchez et al. 1992).

Finally, even with all theses corrections, we must remember to be very careful when interpreting satellite data because of all unresolved or insufficiently modeled errors.

### **3. Delimitation of the study and plan of investigation**

A long file of residual heights along with its respective time, location and track number is now available for further studies. Figure 22 shows the satellite ground tracks in



the investigated area. With such data, the investigation of short time scale processes was impossible. The exact repeat of the satellite provided the same ground track only every seventeen days and the data were missing during certain periods. Due to the sampling rate, the distance between each observation is greater than 5 kilometers, so the altimeter sampling scale is greater than the small scale plumes of the deep convection.

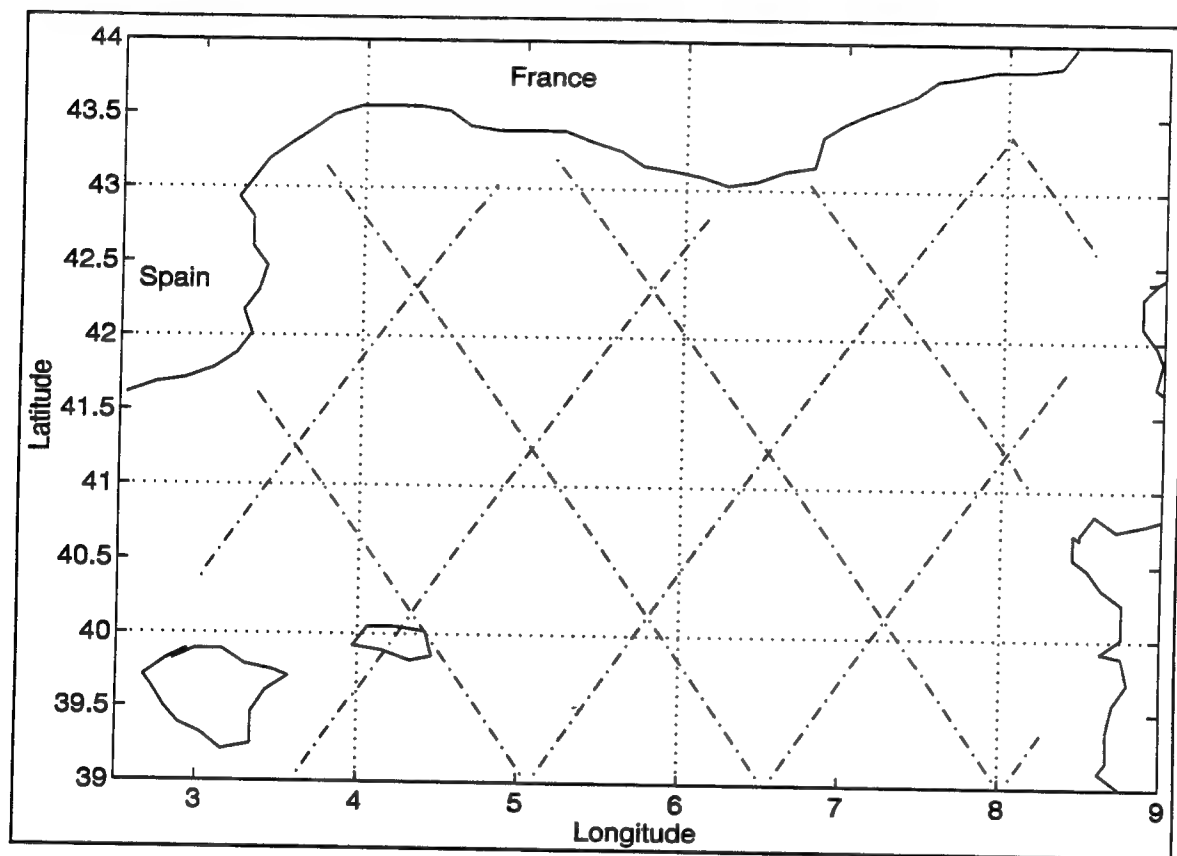


Figure 22. The Area of Investigation and the GEOSAT Ground Tracks Used.

However, a monthly study of the global variation of the sea level in a deep convection area is possible. The preconditioning and sinking and spreading phase last a few weeks and can be associated with a sea level change. We will try to look at the large scale ( $O(50-100)$  kilometers) and long term (1 month) process occurring along with or because of the deep convection.

The computation was performed using the following strategy:

- Regroup the data on a monthly basis.
- For each month, compute mean tracks.
- Run an interpolation program in between each mean track, and produce a monthly interpolated height field.
- Produce a movie using the 24 interpolated frames.

#### **4. Producing monthly interpolated frames**

##### ***a. Monthly mean frames***

The first step of the computation was to regroup the data on a monthly basis. The time of the sampling, given in seconds and referenced to January 1, 1985 was transformed into the Julian day. In order to simplify the computation, a month was rounded to 30.4 days. Then each line of the data was identified and placed into its respective monthly frame. This produced twenty four frames (November 1986 to October 1988), each frame containing 5 to 16 tracks.

Within each frame, the collinear tracks have been regrouped by identifying the track number available for each sampling. For each track number, all the data were read. Often the track was recorded twice, so it was necessary to remove duplicated data. If two similar times were found, one of them was discarded. The remaining collinear data were averaged.

To compute a mean height along each collinear track, latitude is used as the reference axis, each track was divided into 1/10 degree bins (Fig. 23). Within each bin the latitude, longitude and height were averaged to produce one mean track (mean latitude, longitude and height every 1/10 degree).

For each track, from one frame to another, the mean latitude and the mean longitude vary generally less than 0.05 degree (approximately 4 kilometers). Thus, it is reasonable to hypothesize that over the frames, each track has an identical ground signature and therefore confirm that the cross track error is minimal in regions where the geoid has little gradient.

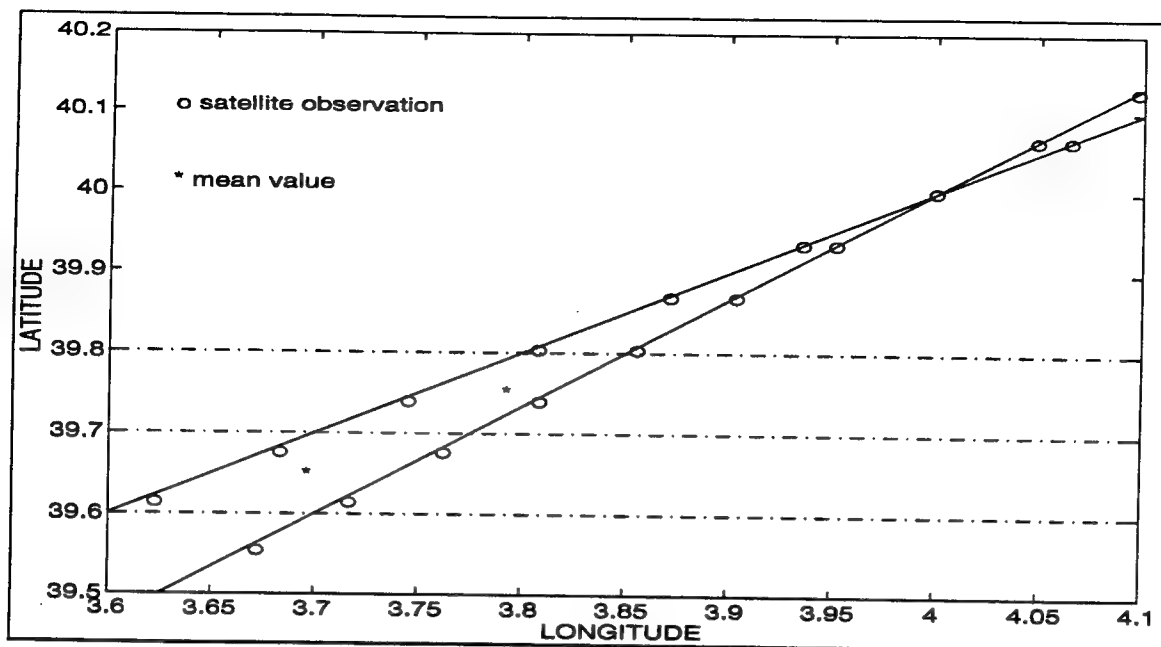


Figure 23. The Principle of Averaging Two Collinear Tracks.

This computation produced 24 frames each containing 5 to 10 tracks with averaged residual heights.

***b. The interpolation process***

The field is sampled only at particular locations. We need an interpolation program to cover the entire domain. A multiquadric interpolation program developed Chumbinho (1993) following a method provided by Nuss (1993) was available.

For each sampled location, the ground track (latitude, longitude) and the value of the surface ( $H$ , residual mean height) is known. The interpolation of the surface in any arbitrary point  $X$  is based on a weighted sum of radial basis functions:

$$H(X) = \sum_{i=1}^N \alpha_i Q(X - X_i) \quad (4.5)$$

$\alpha_i$  being the weight of the kernel function  $Q$ , and its argument the radial distance between the point  $X$  and the observation point  $X_i$ .

For multiquadric interpolation, the kernel function is a hyperboloid function:

$$Q(X_i - X) = [(X - X_i)^2 + c^2]^{1/2} \quad (4.6)$$

The constant  $c$ , an arbitrary small number, precludes the function from vanishing at the observation point.

Equation 4.5 is applied to all  $N$  observation points to solve for the weights producing a set of  $N$  equation with  $N$  unknowns.

$$H_j = H(X_j) = \sum_{i=1}^N \alpha_i Q_i(x_j, y_j) \quad (4.7)$$

The  $Q$  matrix is inverted to yield the weights that in turn provide the interpolated solution at any regularly spaced grid point:

$$H_g = Q_{gi} \alpha_i \text{ where } Q_{gi} = [(x_g - x_i)^2 + (y_g - y_i)^2 + c^2]^{1/2} \quad (4.8)$$

where  $(x_g, y_g)$  are the coordinates of each regular grid point. The solution depends only on the number of observation points available and is independent of the size of the grid to be interpolated.

To account for noisy observations an uncertainty parameter and a smoothing coefficient are introduced in the diagonal element of the kernel function (Nuss and Title 1993).

$$H_j = Q_{ij} + [N * \lambda * \sigma_i^2 * \delta_{ij}] * \alpha_i \quad (4.9)$$

where  $\delta_{ij}$  is the Kronecker delta function,  $\sigma_i^2$  is the smoothing coefficient and  $\lambda$  is a vector of uncertainties in the observations (mean-squared observation error).

***c. Searching the best interpolation coefficients***

Choice of the best smoothing parameter and coefficient  $c$  is somewhat subjective. The damping of the field is controlled by the smoothing parameter; large values cause a strongly damped solution. The constant parameter determines the shape of the interpolated field; large values of  $c$  imply a rather flat interpolating function, and tight gradients or closely spaced observation points may be misrepresented. The table below summarizes the different choices applied in conjunction with Fig. 26.

	LARGE LAMBDA	SMALL LAMBDA
LARGE C	Field strongly damped. Misrepresentation of a tight gradient.	Real field. Misrepresentation of a tight gradient.
SMALL C	Field strongly damped. Good representation of a tight gradient.	Real field. Good representation of a tight gradient.

Table 2. Influence of the Interpolation Coefficients on the Field Produced

Inappropriate values of the smoothing parameter create an unrealistic interpolated field. The initial heights show many bumps along their tracks that need to be smoothed. However, the general shape of the field must be preserved without too much damping or contamination by false data created during the interpolation (black spots on the plots are points out of range). As it can be seen on Fig. 26, using different pairs of parameters leads to different interpolation fields. The pair chosen for the study is the best trade-off possible with a medium constant parameter ( $c=10^{-2}$ ) and a small smoothing coefficient ( $\lambda=10^{-3}$ ). This allows reasonable representation of the general gradient.

## D. RESULTS

For each of the two runs, the full area and a zoom over the area of interest (100 kilometers around the center of deep convection:  $42^{\circ}\text{N} - 5^{\circ}\text{E}$ ) were presented. In the first, the averaged heights were used without smoothing. In the second case, for every month, a mean shape was visually extracted from each individual track. This was done to reduce the bumps found on each tracks, because the sea surface rarely has steep gradients. The plots are presented at the end of this chapter.

### 1. The averaged heights

#### *a. Interpretation of the results*

Looking at the global area (north part of the Northwestern basin), there is unfortunately no direct correlation apparent between the deep convection and the evolution of the sea surface level (Fig. 27, 28, 29 and 30). Except for a small feature in the northwest of the first three frames, there is no obvious common feature that could be seen when playing the movie made with the monthly frames. There is also no direct comparison from one year to the next. The rise and fall of the sea level neither occur at the same location nor at the same time in the year.

However, this small feature deserves a special attention (Fig. 30). During the three months prior to the convection period (November 1986, December 1986 and January 1987) there is a significant deepening close to the estimated location of the convection ( $42^{\circ}\text{N} - 5^{\circ}\text{E}$ ) which happens to be along satellite track 487. The elevation of the convection area (100 kilometers around that location) is lower from November to January and appears slightly higher afterwards. This late winter deepening may be linked with the preconditioning phase and the early spring rising with the spreading phase, when the water rises slowly from the bottom.

Looking at that particular track (Fig. 31), the presence of the low can be seen in almost all of the passes and seems to be moving between  $41.5^{\circ}\text{N}$  and  $42^{\circ}\text{N}$ . Since it appears on the original tracks, the feature is not a series of false data created by the program, so it can be interpreted as a real phenomenon.

### ***b. Comparison to in-situ observations***

How does the above discussion relate to the investigation of Schott and Leaman (1991)? The position of their mooring was based on the supposed location of the center of the deep convection; they also conducted CTD observations up to 60 kilometers from the center to determine the hydrographic structure within the convection zone. Their data cover only the convective period (mid January 1987 to mid March 1987) and the closest satellite tracks only sample the southern portion of their zone of investigation (tracks 487 and 160). A direct comparison for the global area is difficult; however, the position of the feature discussed earlier coincides with the southern limit of the deep-mixed patch (salinity  $> 38.4$ ) found by Schott and Leaman (Fig. 32). Part of the signature of this heavier water could be the low seen in the satellite interpolated field.

#### **2. The smoothed tracks**

To reduce the bumps in the sea surface heights, a mean shape was visually extracted from each individual track. This was done to try to reveal the large scale feature. The interpolated field built with these smoothed tracks is flatter than before (Fig. 33) and highs and lows are now easily identifiable. As with the previous field, it is not possible to firmly associate the evolution of the convective patch with some of the images. The previous interesting feature shows up only in January 1987 but it is now larger. The smoothed tracks do not bring any additional information.

#### **3. The averaged winter frame**

A final and probably better use of these frames can be made by averaging all the winter frames and comparing them to the mean winter surface density field. From the analysis of historical data (1905 to 1988) a winter sea surface density field was deduced (F. Aikman III, personal communication) which helps to define the extend, as seen in Fig. 34, of the deep water formation in the Northwestern Mediterranean sea (Madec et al. 1991).

Frames from November to March were used to produce a mean sea level field that shows a characteristic slope toward the north (Fig. 35). The blue oval shape area

refers to a mean low that is fairly consistent with the limits of the heavier water. As we go south, the color changes from blue to yellow, meaning that the sea level increased. This also means that the water is becoming less dense. The blue area is slightly higher in latitude than the historical data field but our computation uses only two years of data instead of 83 and there are still unresolved errors.

#### **E. PARTIAL CONCLUSION AND RECOMMENDATIONS**

For the large area and the two year period covered, it is not possible to extract the location and the extent of the deep convection, nor firmly identify it in time. However, knowing that there was a deep convection event, there is a small feature found over three months in the northwest of the remotely sensed area which could be related to the low in the sea surface. A correlation with in-situ data is possible.

The sum of the residual errors and the insufficient spatial and temporal resolution prevent the observation of the typical deep convection lows. The tidal and inverse barometer errors which are not taken into account and the orbital error which is difficult to estimate are certainly major handicaps.

We can go further in the investigation only if we possess the correct tools in terms of satellite instruments. An increase the spatial and temporal resolution are strongly required in order to see small-scale and short-period phenomena that might be identify as deep convection. The TOPEX/POSEIDON altimeters will probably give a significant improvement to the remote sensing of oceanic convection and related mesoscale features.



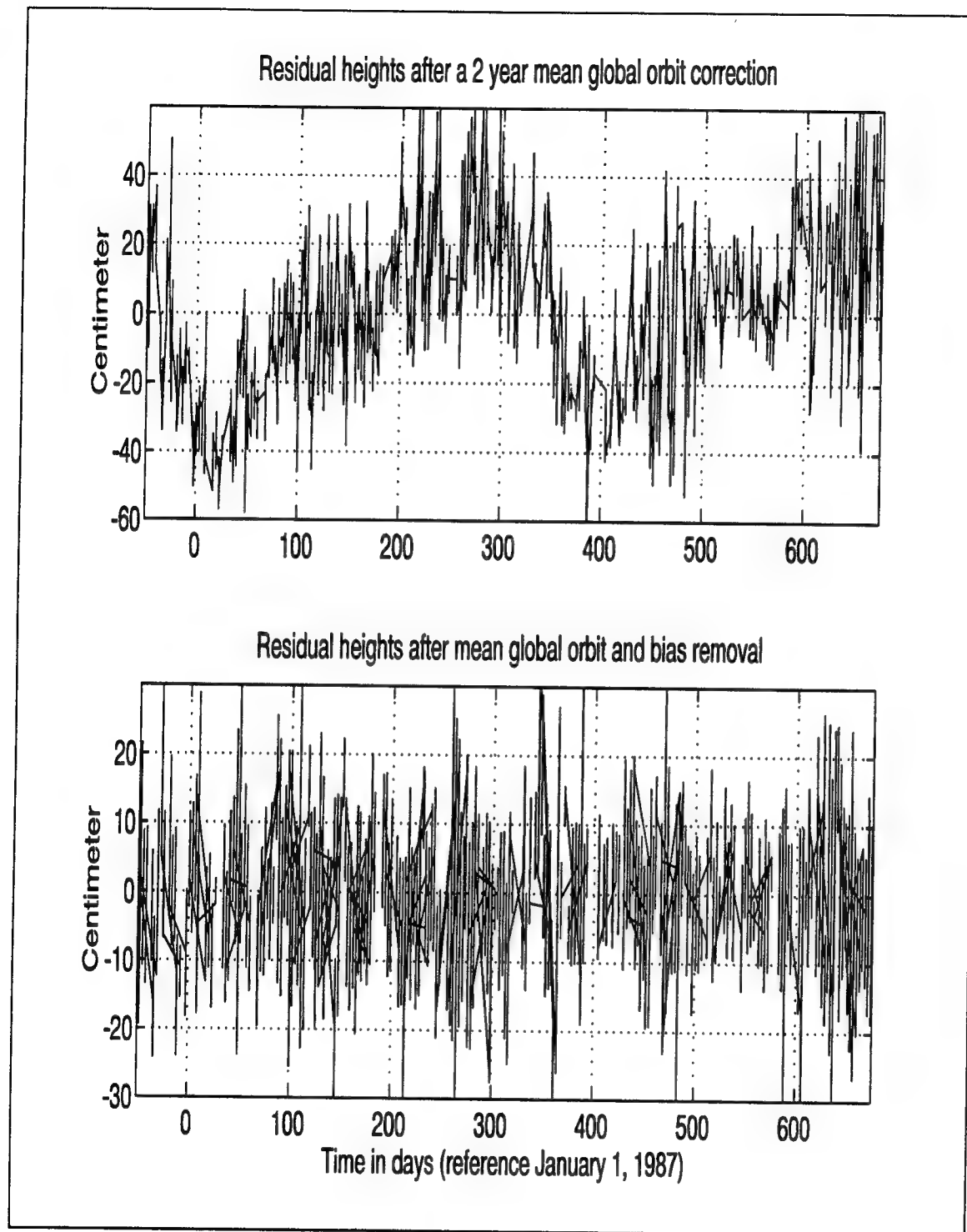


Figure 24. The Residual Heights after the Two Year Mean and Bias Removal.

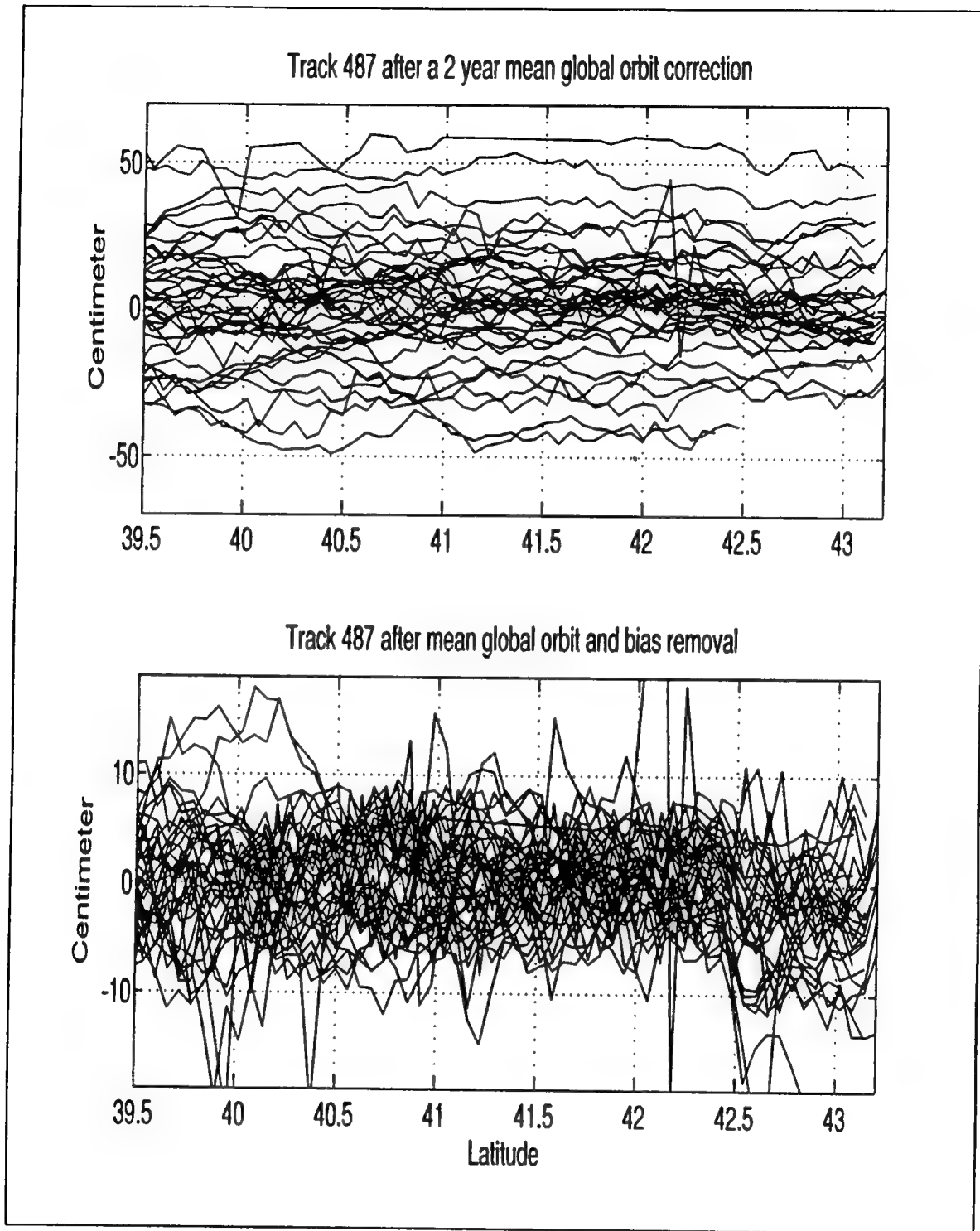


Figure 25. The Residual Height of Track 487 after the Two Year Mean and Bias Removal.

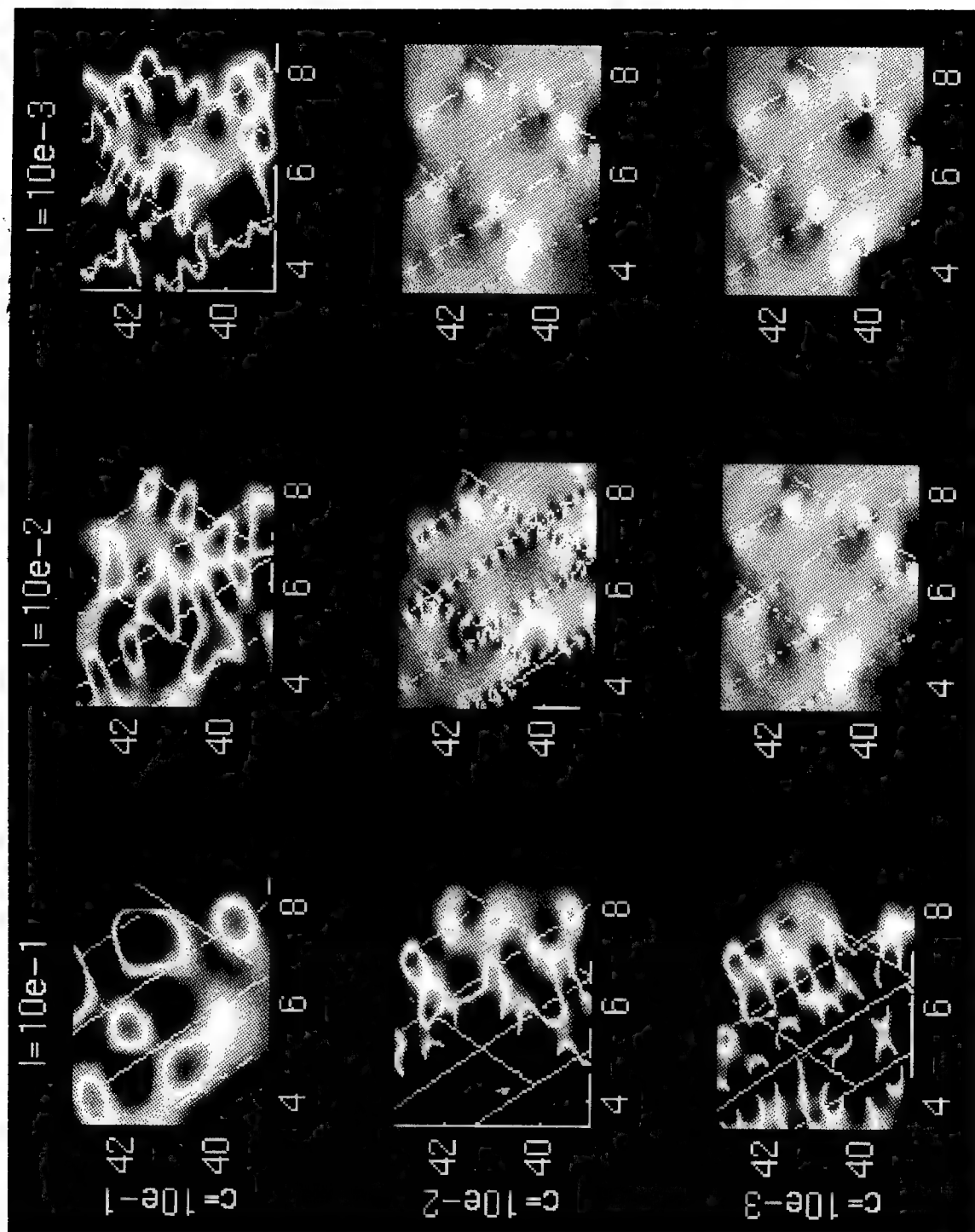


Figure 26. The Influence of The Multiquadric Interpolation Parameters on the Interpolated Field.

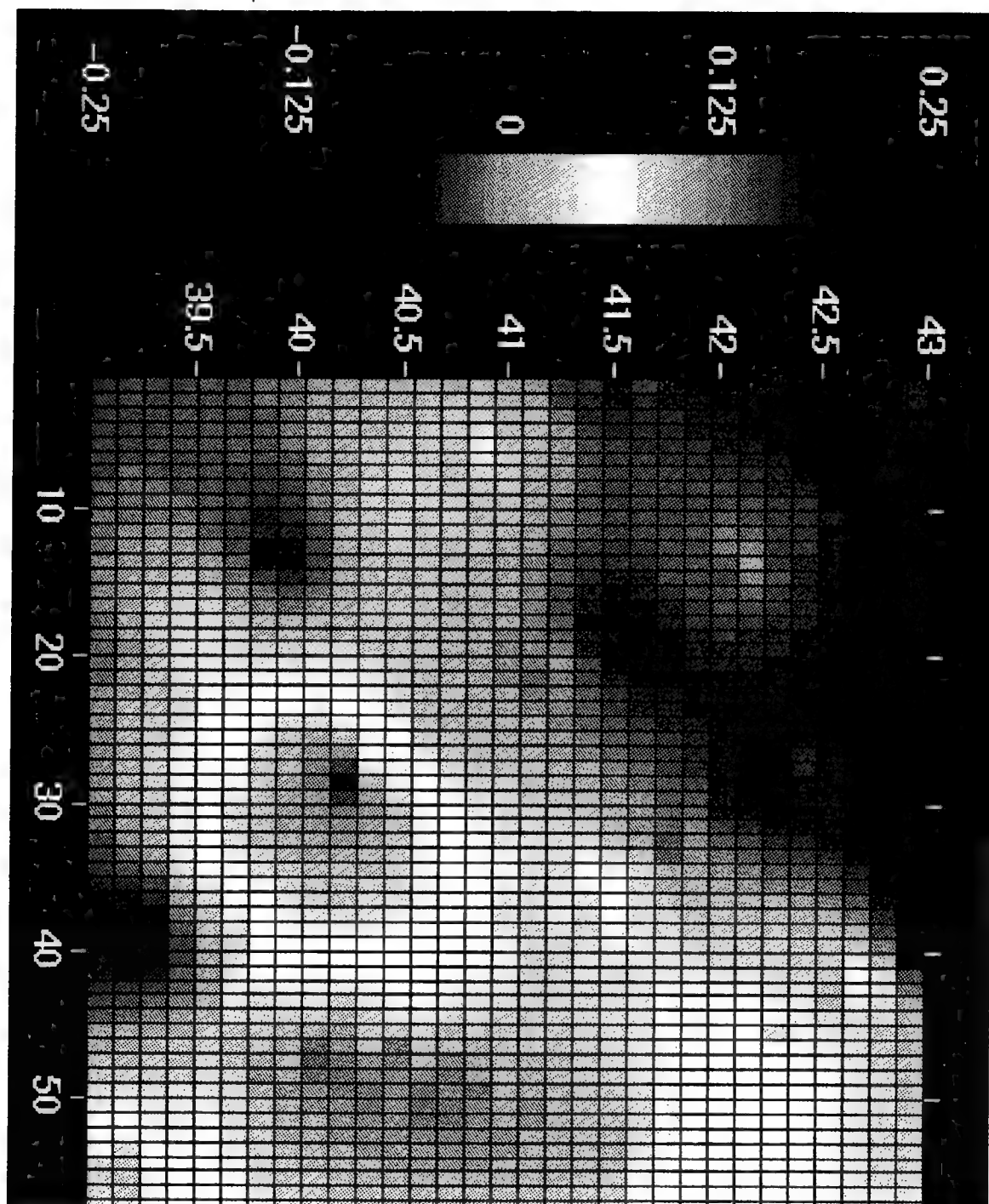


Figure 27. Monthly Frames (November 1986 - July 1987) of Interpolated Field Produced with Averaged Heights (Scale in Meter).

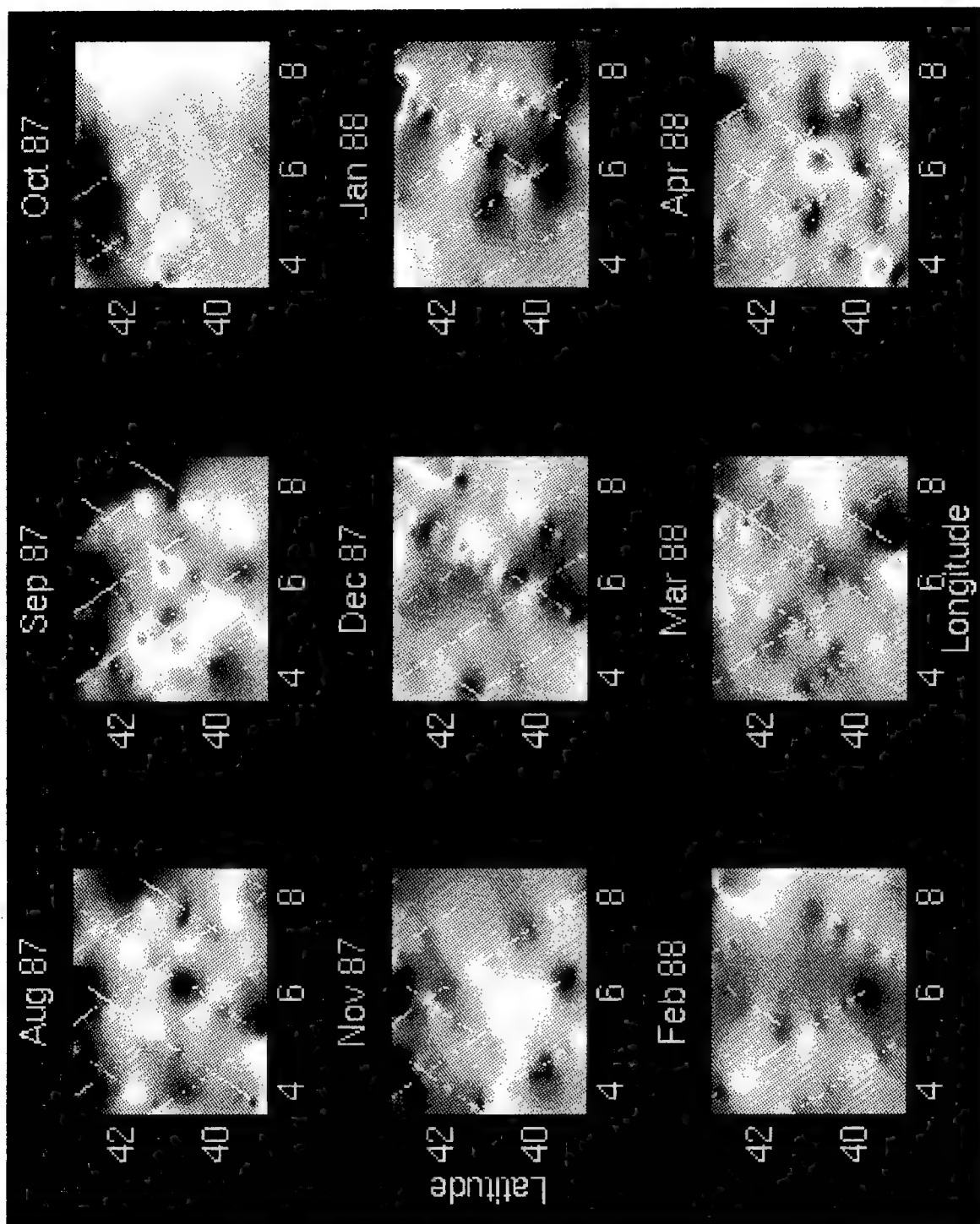


Figure 28. Monthly Frames (August 1987 - April 1988) of Interpolated Field Produced with Averaged Heights.

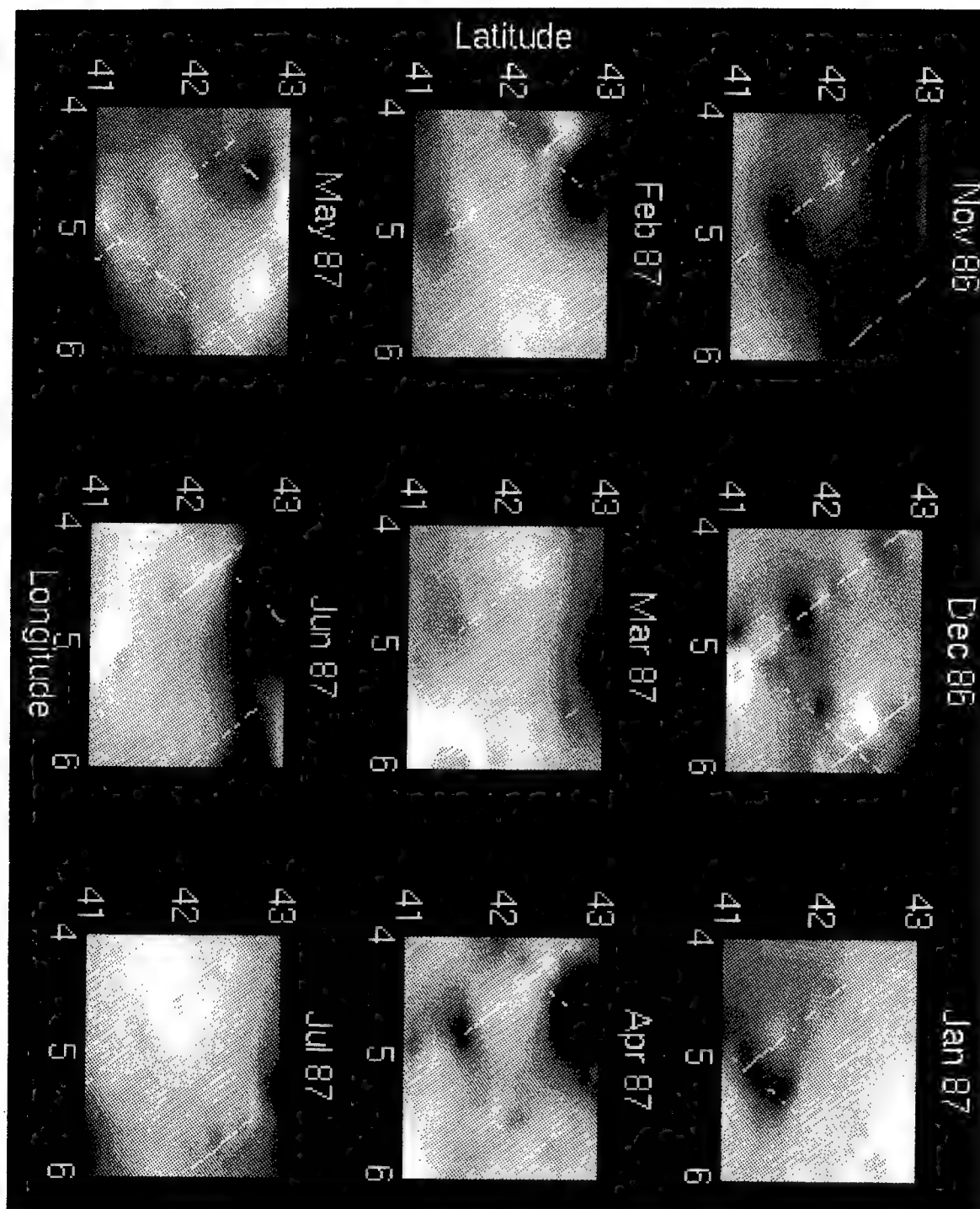


Figure 29. Zoom of the Convection Area (November 1986 - July 1987) of Interpolated Field Produced with Averaged Heights.

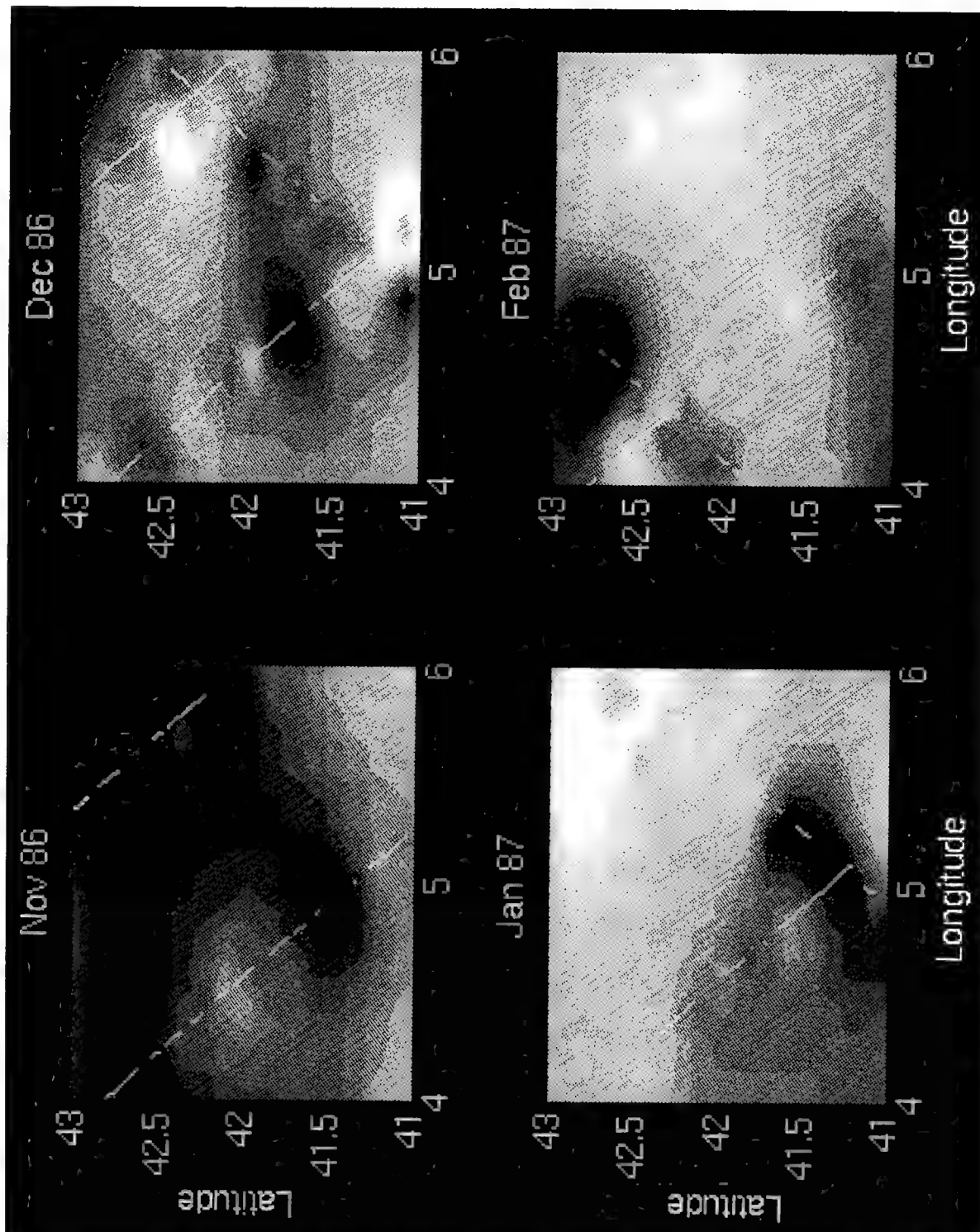


Figure 30. Same as Fig. 29 but for the Period November 1986 - February 1987.



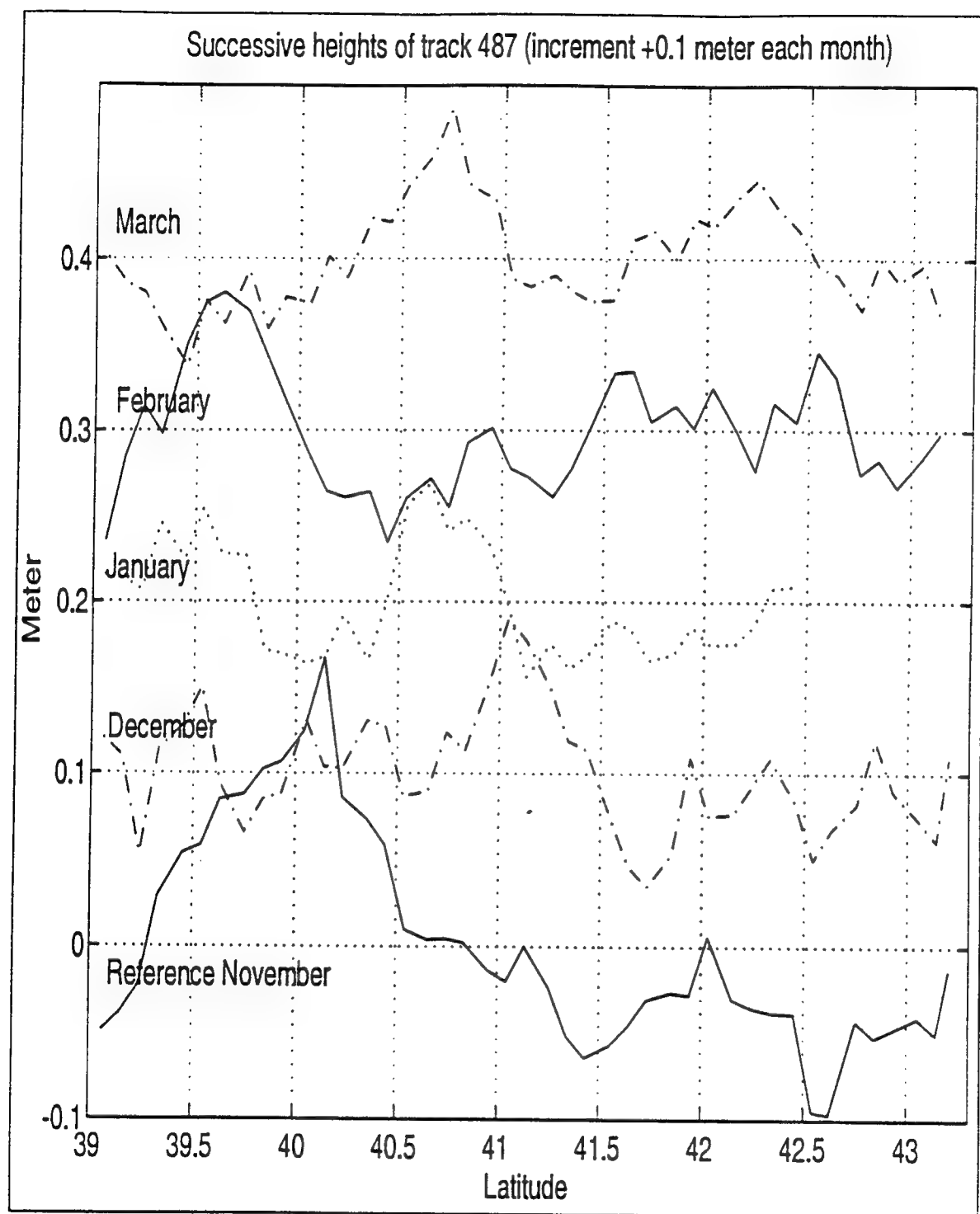


Figure 31. Time Series of the Track 487 (November 1986 - February 1987).



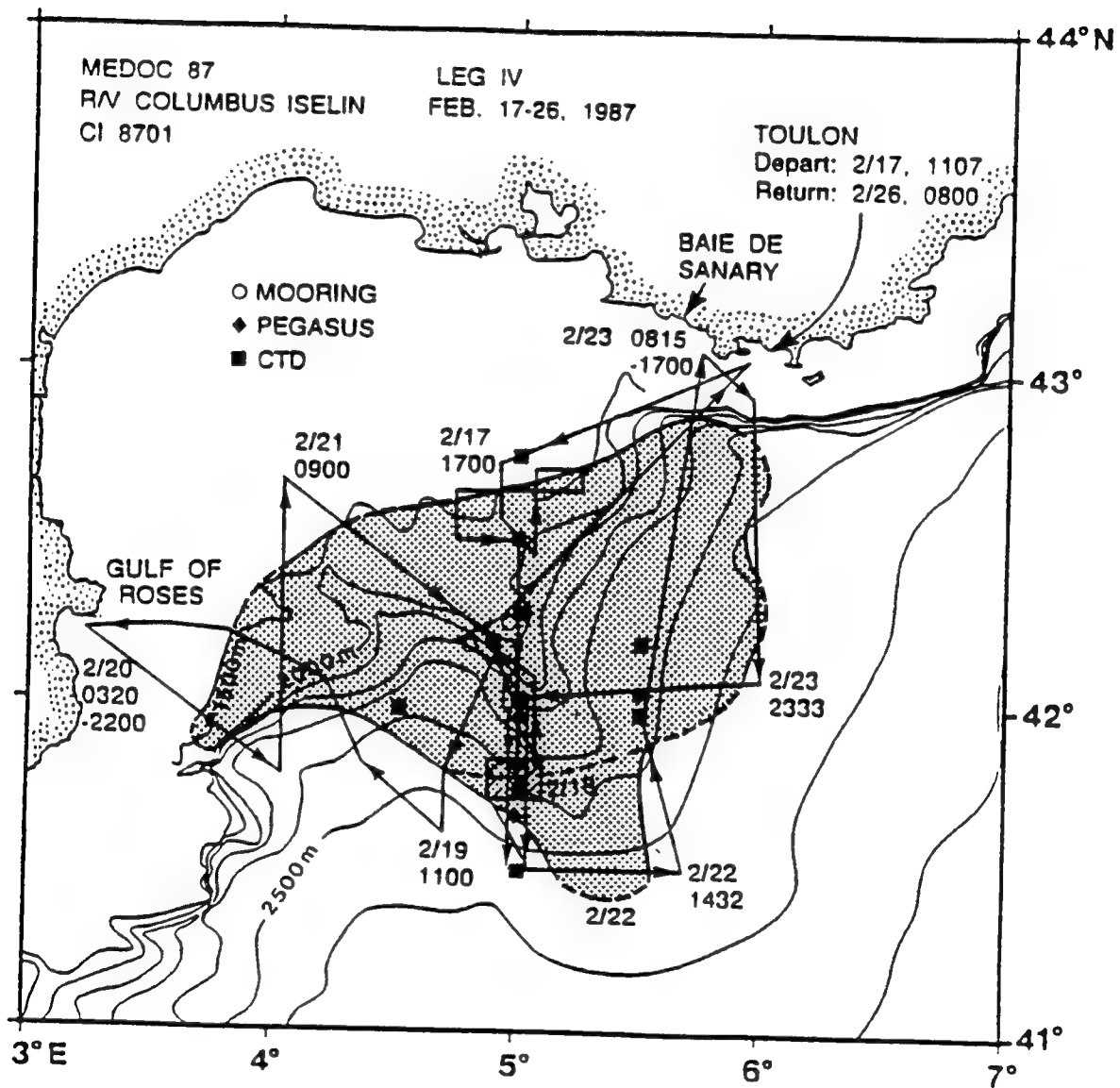


Figure 32. The Deep Mixed Path inside the Convection Area during the Convection Period. From Leaman and Schott 1991.

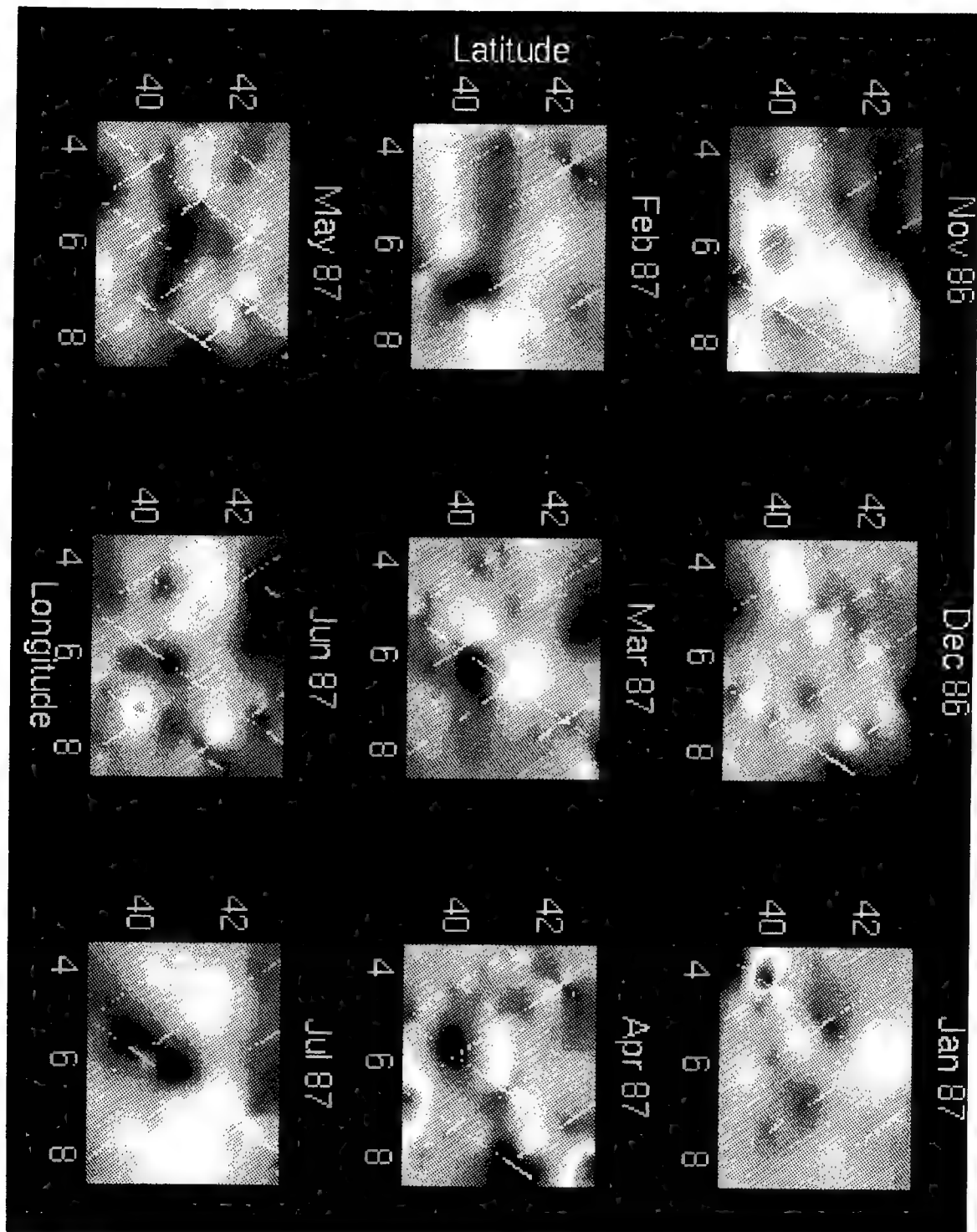


Figure 33. Monthly Frames (November 1986 - July 1987) of Interpolated Field Produced with Smoothed Heights.

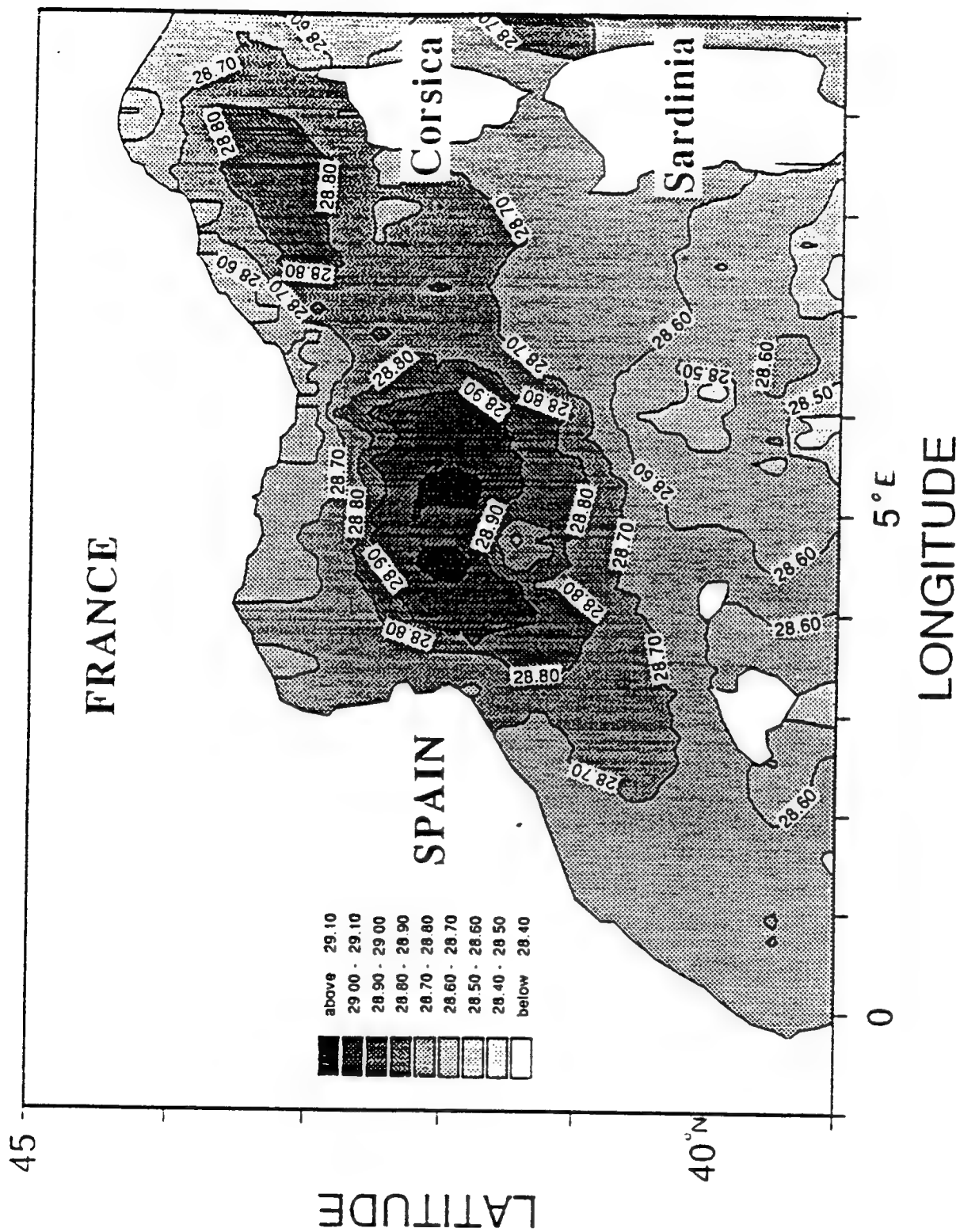


Figure 34. Sea Surface Density in Winter from Historical Data. From Madec et al. 1991.

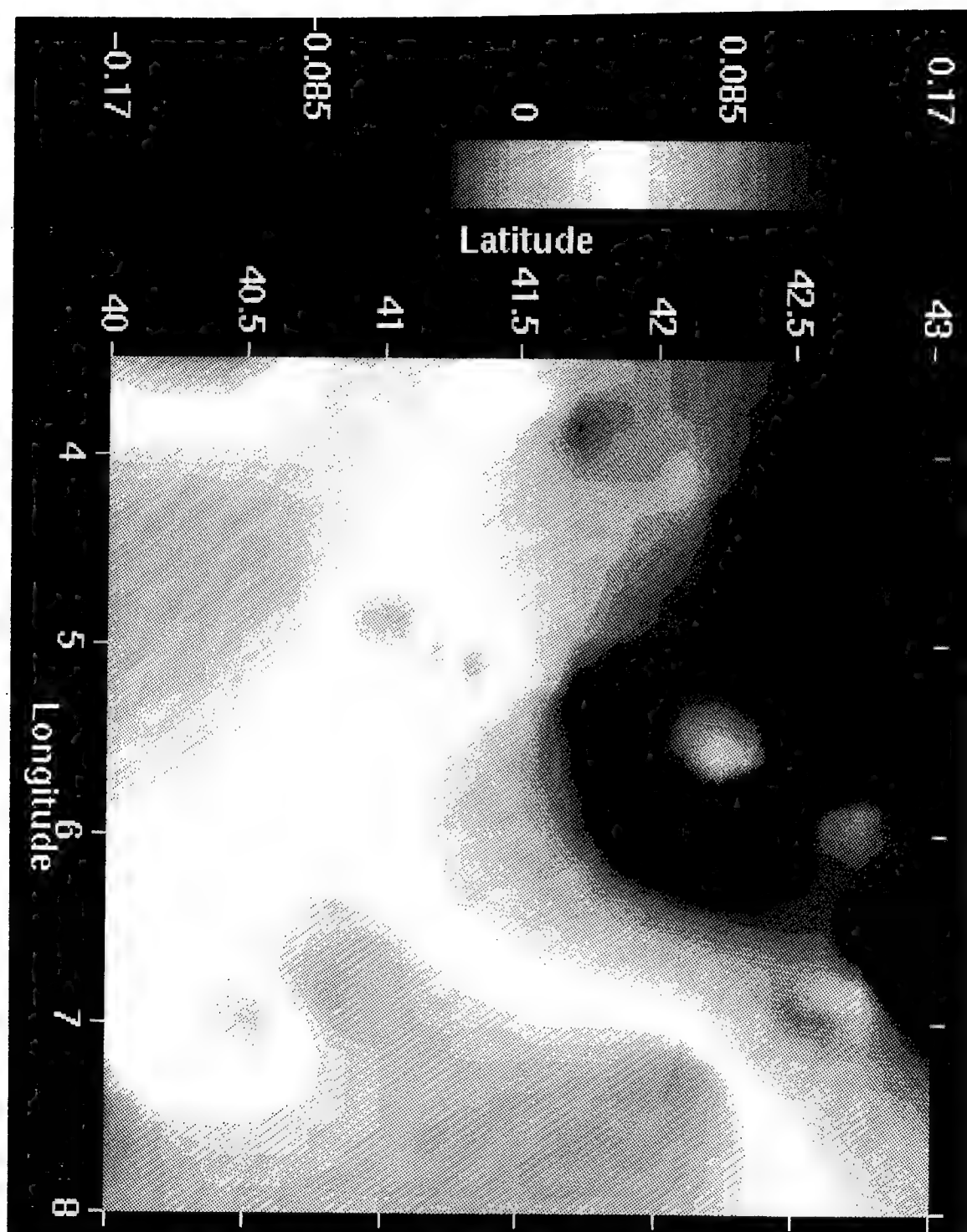


Figure 35. Mean Winter Interpolated Altimeter Field.

## V. CONCLUSION

The first part of this research investigated the behavior of the Kraus and Turner and the Naval Postgraduate school mixed layer models under deep convection conditions. These models were initialized with observed temperature and salinity profiles and were run under the observed forcing. With the tuning coefficients set for a nonconvective mixed layer deepening (original set of coefficients), both models produce final values of temperature and salinity similar to observations. However, the mixed layer depth only reached 1150 meters with the Kraus and Turner model and 500 meters with the Naval Postgraduate School model after ten days of forcing. The swiftness of the deep convection process (a few hours in the observed case) can be approached by adjusting the coefficients. In that case, the Naval Postgraduate School model provides the best simulation and reaches the bottom and the observed temperature and salinity deep convection values after three days.

The changes in the coefficients are required by the convection process, but a physical justification can be made for only two of them. A complete justification of the coefficients can be done with higher order convection models and the Large Eddy Simulation model may be used to better understand the physics of deep convection.

An investigation of deep convection by remote sensing instruments has been conducted in the second part of this research. The identification of this process with an interpolated altimeter field is still not possible on a global temporal and spatial scale. There is no strong signature of the deep convection process. The required signal magnitude is slightly higher than the precision of the measurement, and some errors are still present. However, a persistent low in the sea level at the location of the deep convection area and in the mean winter altimeter field are consistent with in-situ observations and provide some hope in studying and later identifying this phenomenon from space. With the recent altimeters, such as those on the joint United-States/France TOPEX/POSEIDON mission, we may now have a tool to answer this investigation.

## LIST OF REFERENCES

- Arabelos, D. and Tziavos I. N., Sea Surface Heights in the Mediterranean Sea from Geosat Altimeter Data. *Journal of Geophysical Research*, pp. 17947-17956, vol. 95, 1990.
- Carsey, F.D. and Garwood R.W. Jr., Identification of Modeled Ocean Plumes in Greenland Gyre Ers-1 Sar Data. *Geophysical Research Letters*, pp. 2207-2210, vol. 20, No.20, 1993.
- Chu P.C. and Gascard J.C., *Deep Convection and Deep Water Formation in the Oceans*, Elsevier Science Publishers B.V, 1991.
- Chumbinho, R. P. A., *Objective Analysis of a Coastal Ocean Eddy using Satellite AVHRR and In-Situ Data*, Master's Thesis, Naval Postgraduate School, Monterey, Ca, 1993.
- Hogg, N.G., The Preconditioning Phase of Medoc 1969. Part II: Topographic Effects. *Deep Sea Research*, pp. 449-459, vol. 20, 1973.
- Garwood, R. W. Jr, An Oceanic Mixed Layer Model Capable of Simulating Cyclic States. *Journal of Physical Oceanography*, pp. 455-468, vol. 7, 1977.
- Garwood, R.W. Jr, Enhancements to Deep Turbulent Entrainment, *Deep Convection and Deep Water Formation in the Oceans*, Elsevier Science Publishers B.V, 1991.

- Garwood, R.W. Jr, Isakari S. M. and Gallacher P.C., *Thermobaric Convection. The Role of the Polar Oceans in Shaping the Global Environment*, Edited by Johannessen O., Muench R. and Overland, AGU Monograph, in Press, 1994.
- Gascard, J. C., Vertical Motions in a Region of Deep Water Formation, *Deep-Sea Research*, pp 1011-1027, vol. 20, 1973.
- Gascard, J.C., Mediterranean Deep Water Formation, Baroclinic Instability and Oceanic Eddies. *Oceanology Acta*, pp. 315-330, vol. 1, no 3, 1978.
- Johns Hopkins APL Technical Digest. *The Navy Geosat Mission*, vol. 8, no. 2, April-June 1987.
- Killworth, P. D., The Mixing and the Spreading Phase of Medoc 1969, *Progress in Oceanography*, Pergamon, pp. 59-90, vol. 7, 1976.
- Kraus, E. B. and Turner J. S., A One-Dimensional Model of the Seasonal Thermocline, Part II, *Tellus*, pp. 98-105, vol. 19, 1967.
- Leaman, K. and Schott F., Hydrographic Structure of the Convection Regime in the Gulf of Lions: Winter 1987, *Journal of Physical Oceanography*, pp. 575-597, vol. 21, 1991.
- Madec, G. , Chartier M., Delecluse P. and Crepon M., A Three Dimensional Numerical Study of Deep Water Formation in the Northwestern Mediterranean Sea. *Journal of Physical Oceanography*, pp. 1349-1370, vol. 21, 1991.
- Matlab, *Matlab User's Guide*, Version 4.0, The Mathworks, 1992.

- Medoc Group 1970, Observation of Formation of Deep Water in the Mediterranean. *Nature*, pp. 1037-1040, vol. 227, 1970.
- Moeng, C.-H., A Large-Eddy Simulation Model for the Study of Planetary Boundary Layer Problems. *Journal of Atmospheric Science*, pp. 2052 - 2062, vol. 41, 1984.
- Nuss, W. A., *Three Dimensional Meteorological Analysis using Multiquadric Interpolation*, Unpublished, 1993.
- Nuss, W. A., and Titley D. W., Use of Multiquadric Interpolation for Meteorological Objective Analysis, Paper submitted to *Monthly Weather Review*, 1993.
- Paluszkievicz, T., Garwood R. W. Jr, and Denbo D. W., Deep Convective Plumes in the Ocean, *Oceanography*, 7, in press 1994.
- Pickard, G. L. and Emery W. J., *Descriptive Physical Oceanography: An Introduction*, Pergamon Press, 1990.
- Sanchez, B. V., Ray R. D., and Cartwright D. E., A Proudman-Function Expansion of the M2 Tide in the Mediterranean Sea from Satellite Altimetry and Costal Gauges, *Oceanologica Acta*, pp325-337, vol. 15 no. 4, 1992.
- Schott, F. and Leaman K. D., Observations with Moored Acoustic Doppler Current Profilers in the Convection Regime in the Golfe du Lion, *Journal of Physical Oceanography*, pp. 558-574, vol. 21, 1991.
- Stewart, R. H., *Methods of Satellite Oceanography*, University of California Press, 1985.



Swallow, J. C., and Gaston G. F., The Preconditioning Phase of Medoc 69. Part I : Observations. *Deep-Sea Research*, pp. 429-448, vol. 20, 1973.

Vaughan, S.L, *The Role of Small Scale Cells in the Mediterranean Convection Process*, Phd Dissertation, University of Miami, 1993.

Voorhis, A. D., and Webb D.C., Large Vertical Currents Observed in a Winter Sinking Region of the Northwestern Mediterranean. *Cahiers Oceanographiques*, pp. 571 - 580, vol. 22, 1970.

## INITIAL DISTRIBUTION LIST

- |   |       |
|---|-------|
| 1. Defense Technical Information Center | 2     |
| Cameron Station                         |       |
| Alexandria, VA 22304-6145               |       |
| <br>2. Library, Code 52                 | <br>2 |
| Naval Postgraduate School               |       |
| Monterey, CA, 93943-5002                |       |
| <br>3. Oceanography Department          | <br>1 |
| Code OC/Bf                              |       |
| Naval Postgraduate School               |       |
| Monterey, CA, 93943                     |       |
| <br>4. Dr. Roland W. Garwood            | <br>3 |
| Code OC/Gd                              |       |
| Naval Postgraduate School               |       |
| Monterey, CA, 93943                     |       |
| <br>5. Dr. Newell Garfield              | <br>1 |
| Code OC/Gf                              |       |
| Naval Postgraduate School               |       |
| Monterey, CA, 93943                     |       |

- |   |   |
|---|---|
| 6. Dr. Robert Haney                           | 1 |
| Code MR/Hy                                    |   |
| Naval Postgraduate School                     |   |
| Monterey, CA, 93943                           |   |
| <br>  |   |
| 7. Arlene Guest                               | 1 |
| Code OC/Gt                                    |   |
| Naval Postgraduate School                     |   |
| Monterey, CA, 93943                           |   |
| <br>  |   |
| 8. Ramsey Harcourt                            | 1 |
| Code OC/Ha                                    |   |
| Naval Postgraduate School                     |   |
| Monterey, CA, 93943                           |   |
| <br>  |   |
| 9. Monsieur l'Amiral                          | 1 |
| Chef d'Etat-Major de la Marine                |   |
| 2 Rue Royale                                  |   |
| 00350 Armées, France                          |   |
| <br>  |   |
| 10. Monsieur le Capitaine de Vaisseau         | 1 |
| Attaché Naval auprès de l'Ambassade de France |   |
| 4101, Reservoir Road, N.W.                    |   |
| Washington, D.C. 20007                        |   |

11. Monsieur l'Ingénieur en Chef de l'Armement 1  
Directeur du Centre Militaire d'Océanographie  
EPSHOM, 13 Rue du Chatellier  
B.P. 426  
29275 Brest Cedex, France
12. Dr. Manuel Fiadeiro 1  
Office of Naval Research  
Code 322PO  
800 N. Quincy Street  
Arlington, VA, 22217
13. Dr. Friedrich Schott 1  
Institut für Meereskunde an der Universität Kiel,  
Dusternbrooker Weg 20,  
Kiel, Germany.
14. Dr. Martin Wisbeck 1  
Center for Meteorology and Physical Oceanography  
Massachusetts Institute of Technology  
Department of Earth, Atmospheric and Planetary Sciences  
Cambridge, MA 02139
15. Dr. Theresa Paluszkievicz 1  
Pacific Northwest Laboratory  
Batelle, 439 West Sequim Bay Road  
Sequim, WA, 98382

- |  |   |
|--|---|
| 16. Dr Shari Vaughan                         | 1 |
| AOML, NOAA                                   |   |
| 4301, Rickenbacker Crossways                 |   |
| Miami, FL, 33149                             |   |
|  |   |
| 17. Monsieur le Lieutenant de Vaisseau Arata | 1 |
| Cellule Opérationnelle d'Environnement       |   |
| 42, Avenue Gustave Coriolis                  |   |
| 31057 Toulouse Cedex, France                 |   |